

# Contents

<b>Introduction</b>	<b>1</b>
<b>1 Nuclear reactors</b>	<b>5</b>
1.1 Nuclear fission process and fission products distribution . . . . .	5
1.1.1 Nuclear fission physics . . . . .	5
1.1.2 Fission cross sections . . . . .	7
1.1.3 Fission products mass distribution . . . . .	10
1.1.4 Nuclear fission energy release . . . . .	11
1.1.5 Burn-up definition . . . . .	12
1.2 Fundamental reactor physics and kinetics parameters . . . . .	13
1.2.1 Prompt and delayed neutrons . . . . .	13
1.2.2 Chain reaction and multiplication factor . . . . .	16
1.2.3 Neutron utilization factor . . . . .	17
1.2.4 Fast fission . . . . .	18
1.2.5 Effective multiplication factor . . . . .	18
1.2.6 Reactor kinetics . . . . .	18
1.2.7 Neutron flux . . . . .	20
1.3 Thermal and fast reactors . . . . .	20
1.3.1 Thermal reactors . . . . .	20
1.3.2 Fast reactors . . . . .	23
<b>2 Fuel burn-up calculations and measurements</b>	<b>27</b>
2.1 Fuel burn-up . . . . .	27

2.1.1	Bateman equations . . . . .	28
30		
2.1.3	Poisons . . . . .	31
2.2	Fuel burn-up calculation codes . . . . .	34
2.3	MCB code: experimental validation . . . . .	34
2.3.1	MCB analytical validation . . . . .	35
2.3.2	MCB experimental validation . . . . .	37
<b>3</b>	<b>Burn-up calculation for the TRIGA Mark II reactor</b>	<b>51</b>
3.1	Experimental facility description . . . . .	51
3.2	Neutron fluxes evaluation . . . . .	55
3.2.1	Specific saturation activity . . . . .	58
3.2.2	Attenuation coefficient . . . . .	59
3.2.3	Flux uncertainties evaluation . . . . .	60
3.2.4	Central channel flux evaluation . . . . .	61
3.2.5	Rabbit channel flux evaluation . . . . .	62
3.2.6	Lazy Susan channel flux evaluation . . . . .	64
3.3	Fuel burn-up analytical evaluation . . . . .	65
3.4	Fuel burn-up calculation using MC codes . . . . .	69
3.4.1	Simulations description . . . . .	70
<b>4</b>	<b>Characterization of the SM1 subcritical Multiplying complex</b>	<b>77</b>
4.1	Experimental facility description . . . . .	79
4.2	Neutron flux simulations . . . . .	82
4.3	Neutron flux measurements . . . . .	83
4.4	Fuel burn-up calculation . . . . .	88
4.4.1	Burn-up analytical evaluation . . . . .	88
4.5	Feasibility study of SM1 conversion to lead fast reactor . . . . .	93
	<b>Conclusions</b>	<b>99</b>
	<b>Appendix: gamma spectroscopy measures</b>	<b>105</b>
	<b>Bibliography</b>	<b>111</b>
	<b>List of publications</b>	<b>117</b>

## CONTENTS

---

**Ringraziamenti**

**119**



# Introduction and keywords

This work of thesis concerns nuclear reactor physics and in particular the burn-up concept: the mass of fissile material consumed only by nuclear fission process. This process is fundamental in a nuclear reactor because it is connected with the reactor performances and safety. During reactor operation, the evaluation of each fuel element burn-up, allows to accomplish the constraints of the plant operation licence while optimizing the core management. At the discharge of fuel, the knowledge of the burn-up is a necessary information in order to plan and to actuate a correct fuel handling and management for the final disposal. In particular the knowledge of burn-up allow the fuel management in the core reactor in order to extend the reactor life.

At the University of Pavia two facilities are present:

- A TRIGA MARK II, a critical research reactor with thermal power  $P=250$  kW at the Laboratory of Applied Nuclear Energy ( LENA).
- SM1, a sub-critical multiplying complex, with thermal power  $P=1$  mW at the Chemistry Department (Radiochemistry Area).

The burn-up calculations are performed at two research facilities: in particular, in order to have a detailed knowledge of this parameter, it is necessary the knowledge of neutron fluxes in each reactor core position. Neutron flux has been evaluated with gamma spectroscopy of irradiated samples and using Montecarlo simulation codes. Burn-up calculations have been performed using the MCB Monte Carlo code (Monte Carlo Continuous Energy Burn-up) which allow to insert the precise geometries and neutron fluxes.

Burn-up calculation of TRIGA MARK II and SM1 experimental facilities is performed within two National Institute of Nuclear Physics (INFN) experiments: ARCO (Analysis of Reactor COre) and NUCSMILE (NUCclear Subcritical Multiplication Installation for Lead Experiment) respectively.

This thesis is divided into four chapters:

- In chapter 1 is reported the nuclear fission mechanism and the nuclear reactor fundamental parameters which are useful in the description of the present work
- Chapter 2 describes the burn-up concept, in particular the Bateman differential equations which governs the time evolution of the fission products and actinides nuclei. In particular in this chapter the analytical and experimental MCB code validation used to calculate the fuel burn-up is described.
- In chapter 3 the TRIGA MARK II experimental facility is described where the neutron flux and burn-up evaluations (analytical and simulated) have been performed. This methodology is validated through the comparison with the reactor *core-excess* measurements.
- In chapter 4 the SM1 experimental facility is described where the neutron flux and burn-up evaluations have been performed.





# Chapter 1

## Nuclear reactors

### 1.1 Nuclear fission process and fission products distribution

#### 1.1.1 Nuclear fission physics

The fundamental process which involves nuclear reactors is the nuclear fission.

Nuclear fission [1] is the process concerning the spontaneous or induced fragmentation of an heavy nucleus into two, or rarely three, lighter nuclei called fission fragments, with the associated production of free neutrons.

In figure 1.1 is shown the average binding energy per nucleon  $B/A$  as a function of mass number  $A$ : it is easy to see why nuclear fission is energetically favorable for heavy nuclei, since  $B/A$  has a maximum of about 8.8 MeV the maximum corresponding to  $^{56}Fe$  and falls down quite slowly with increasing  $A$ . The ratio  $B/A$  is about 7.6 MeV for  $A \cong 240$  region, while it is nearly 8.5 MeV for  $A \cong 120$ .

The binding energy has a fundamental role in the mass calculation of a nucleus with atomic number  $Z$  and mass number  $A$  ( $M(A,Z)$ ):

$$M(A, Z) = ZM_p + (A - Z)M_n - B(A, Z)$$

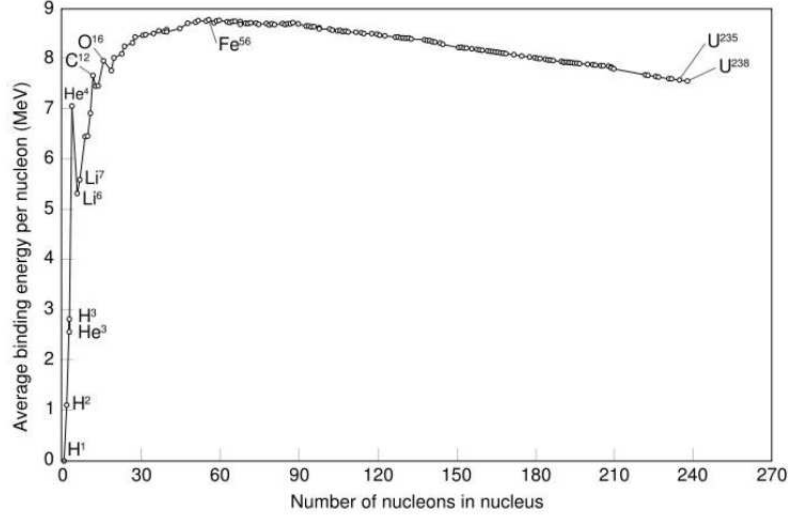


Figure 1.1: Average binding energy per nucleon as a function of number of nucleons

The Weizsacker's semi-empirical mass formula (1.1), gives the nuclear binding energy as a function of mass and atomic numbers  $A$  and  $Z$ ,

$$B(A, Z) = a_V A - a_S A^{\frac{2}{3}} - a_C \frac{Z(Z-1)}{A^{\frac{1}{3}}} - a_A \frac{(A-2Z)^2}{A} + a_P \delta(A, Z) \quad (1.1)$$

where terms with  $a$ 's coefficients represent contributions from nuclei volume, surface, Coulomb energy, asymmetry and even-odd fluctuation,  $\delta(A, Z)$ . The coefficients  $a_V$ ,  $a_S$ ,  $a_C$  are established by fitting the mass-defect curve, respectively [2], [3].

Supposing a fission into two equal fragments, the mass difference  $\Delta M$  between the fissioning nucleus and fragments is given by:

$$\Delta M = M(A, Z) - 2M(A/2, Z/2) =$$

$$a_S(1 - 2^{2/3})A^{1/3} + a_C(1 - 2^{-2/3})\frac{Z^2}{A^{1/3}} - a_S(1 - 2^{1/3})\frac{(N-Z)^2}{A^{1/3}} + \frac{a_P(1 - \delta 2^{3/2})}{A^{1/2}}$$

The process of nuclear fission becomes energetically favorable when  $\Delta M$  is greater than zero (figure 1.2)

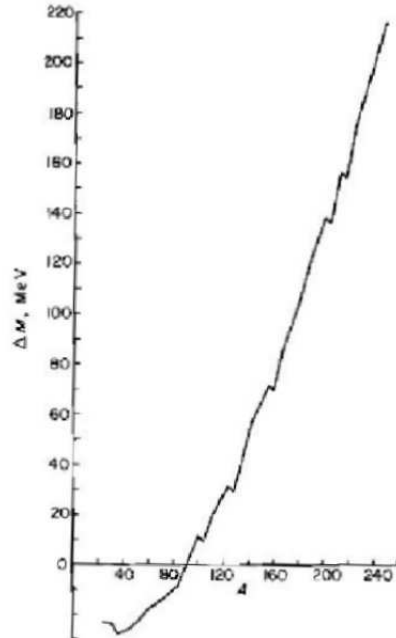


Figure 1.2: Mass difference between fissile nucleus and fission fragments masses

When a neutron is absorbed into an heavy nucleus ( $A, Z$ ) to form a nucleus ( $A + 1, Z$ ), the  $B/A$  value is lower for the compound nucleus than for the original nucleus. For some nuclides (e.g.,  $^{233}\text{U}$ ,  $^{235}\text{U}$ ,  $^{239}\text{Pu}$ ,  $^{241}\text{Pu}$ ), this reduction in  $B/A$  value is such for the compound nucleus to undergo fission, with high probability, even if the neutron has very low energy. Such nuclides are called *fissile* since they can to undergo fission by the absorption of a low-energy neutron (thermal). The neutron kinetic energy is transformed into additional excitation energy of the compound nucleus.

### 1.1.2 Fission cross sections

Fission cross sections for some of the principal fissile nuclides of interest for nuclear reactors are shown in figures 1.3, 1.4 [4]. The resonance structure

corresponds to the formation of excited states of the compound nuclei. The nature of the resonance cross section can be shown to give rise to a  $1/E^{1/2}$  or  $1/v$  dependence of the cross section at off-resonance neutron energies below and above the resonance range, as is evident in these figures. The fission cross sections are largest in the thermal energy region say  $E < 1$  eV. The thermal fission cross section for  $^{239}\text{Pu}$  is larger than that of  $^{233}\text{U}$  and  $^{235}\text{U}$ . Fission cross sections for fertile nuclides  $^{238}\text{U}$  and  $^{240}\text{Pu}$  are shown in figure 1.5 [4] Except for resonances, the fission cross section is about 1 b below about 1 MeV.

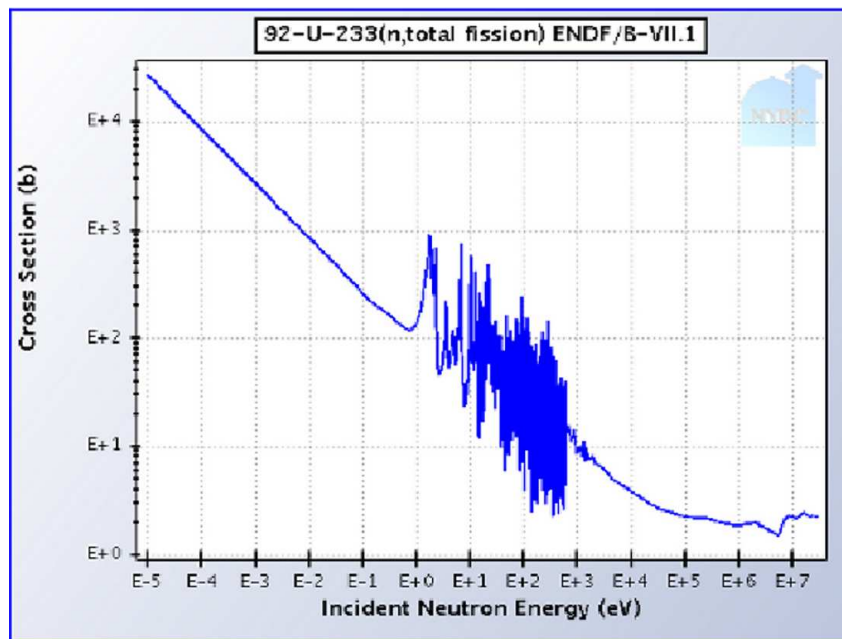


Figure 1.3:  $^{233}\text{U}$  fission cross section as a function of incident neutron energy

It follows that, if a heavy nucleus ( $A \leq 240$ ) splits into two equal fragments, the sum of their masses is less than the mass of fissioning nucleus by  $\Delta = 240(8.5 - 7.6)$  MeV = 216 MeV which is released in form of energy. At the instant of scission, the two fragments are in a highly deformed excited state (figure 1.6).

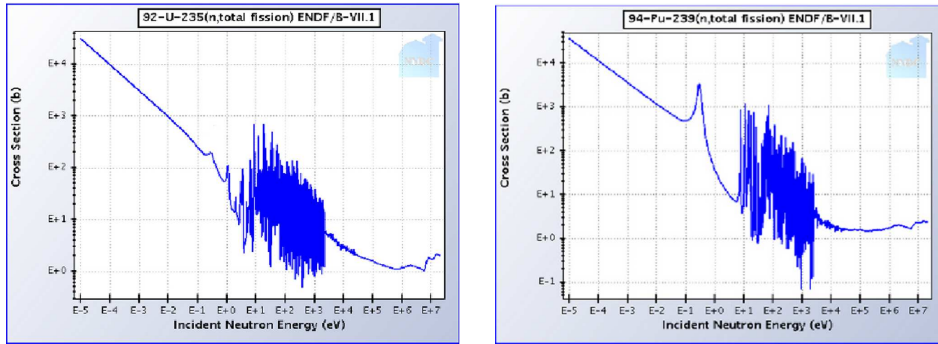


Figure 1.4:  $^{235}\text{U}$  (left) and  $^{239}\text{Pu}$  (right) fission cross sections as a function of incident neutron energy

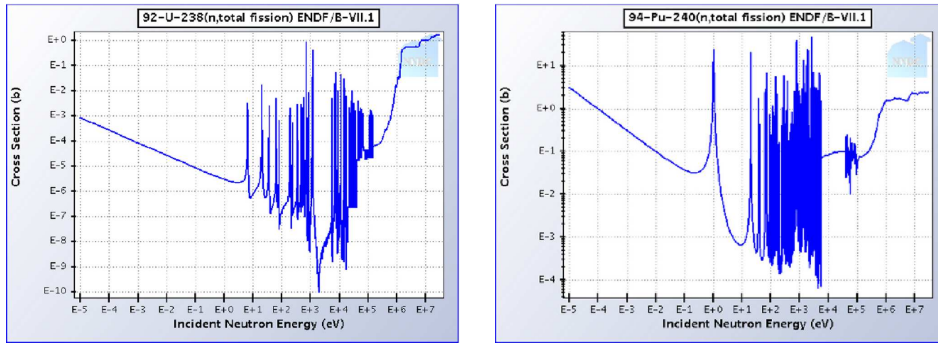


Figure 1.5:  $^{238}\text{U}$  (left) and  $^{240}\text{Pu}$  (right) fission cross sections as a function of incident neutron energy

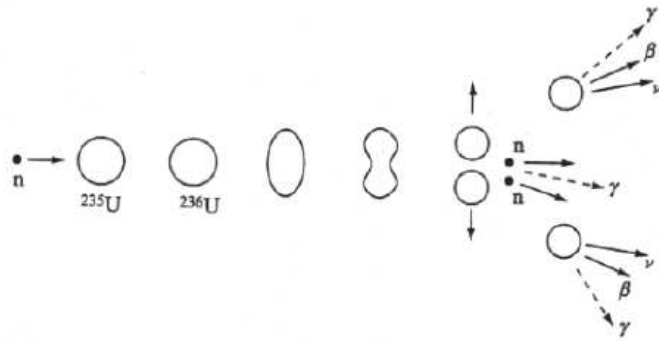


Figure 1.6: Nuclear fission process scheme representing the intermediate step of the nucleus deformation

When the fragments excitation energy has been reduced below the neutron emission threshold, the fragments de-excite by gamma emission with a characteristic time about  $10^{-11}$  s, in order to reach the ground state. Finally the instable fragments (rich of neutrons) decay by  $\beta^-$  emission. In some cases,  $\beta^-$  decay is in energetic competition with neutron emission (delayed neutrons). The percentage of delayed neutrons with respect to prompt neutrons is dependent as the different fissile isotopes. Prompt and delayed neutron issues will be discussed in the next paragraph.

### 1.1.3 Fission products mass distribution

Phenomenologically the fission products mass distribution for  $^{235}\text{U}$  is asymmetric as we can see in the case of thermal and fast (14 MeV) neutrons in figure 1.7. Presence of two peaks around  $A \cong 90$  and  $A \cong 140$  may be seen (it can be different for other fissile nuclei).

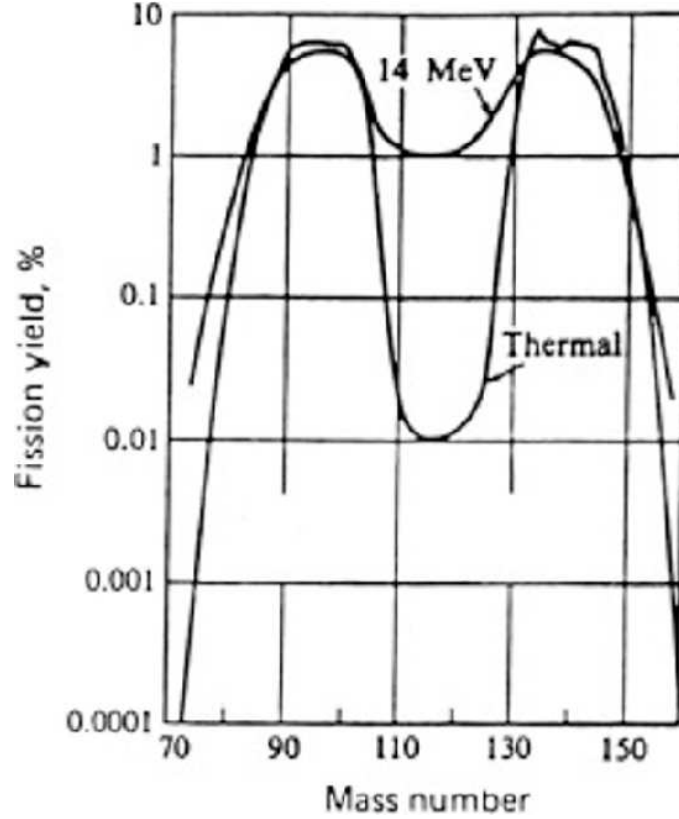


Figure 1.7:  $^{235}\text{U}+n$  fission products mass distribution

From the liquid drop model of the nucleus there are no reasons to expect this asymmetry in fission fragments mass distribution, as shown in (1.1); the asymmetry can be explained by considering shell effects.

As one can see in figure 1.7, an appreciable asymmetry in fission yield starts when one of the fragments has at least 82 neutrons and 50 protons (both magic numbers).

#### 1.1.4 Nuclear fission energy release

During the nuclear fission, an energy  $\cong 210$  MeV is released ( $E_e$ ), but it is not completely recoverable ( $E_r$ ). In table 1.1 is reported the different contributions to the total energy releases:

Form	$E_e$ (MeV)	$E_r$ (MeV)
Fission fragments (k.e.)	168	168
Fission fragments ( $\beta$ rays	8	8
$\gamma$ rays	7	7
Neutrinos	12	0
Prompt $\gamma$ rays	7	7
Fission neutrons (k.e.)	5	5
Capture $\gamma$ rays	0	3-12

Table 1.1: Emitted and recoverable energy from fission

### 1.1.5 Burn-up definition

For the purpose of this thesis the formal definition of burn-up will be introduced.

Let's consider a reactor with thermal power  $P$ (MW), if the energy released during a fission is  $E_R$ (MeV), the fission rate is:

$$R_f = \frac{P(MW)}{E_R(MeV)} \frac{J/MWs}{J/MeV} = 0.312 \times 10^{17} P(MW) s^{-1}$$

The energy release during a fission is, on average,  $E_R=200$  MeV, the daily fission rate may be calculated as:

$$R_D = 86400s/d \times R_f = 2.7 \times 10^{21} P(MW) d^{-1}$$

Fuel *burn-up* is defined as the released energy during fission process in the fuel mass units (calculated as sum of the fissile and fertile material masses). Burn-up is measured in MWd/ton.

If the mass number of the fissile isotope is  $A$ , the daily burn-up rate in terms of fissioned mass is:

$$BU_D = \frac{R_D \times A}{N_A} = 0.895 \times \frac{P(MW)A}{E_R(MeV)} g/d$$

In the case of  $^{235}\text{U}$

$$BU_D = 1.05 \times P(MW)g/d$$

Consumption rate in a thermal reactor, considering neutron capture, is given by:

$$CR_D = 0.895(1 + \alpha) \frac{P(MW)A}{E_R(MeV)} g/d$$

where  $\alpha = \frac{\sigma_{(n,\gamma)}}{\sigma_f}$ .

For a thermal reactor consumption rate is:

$$CR_D = 1.24 \times P(MW)g/d$$

## 1.2 Fundamental reactor physics and kinetics parameters

### 1.2.1 Prompt and delayed neutrons

About two to four prompt neutrons are emitted during the fission process directly from the neutron rich fragments within a time about  $10^{-18}$  s -  $10^{-15}$  s after scission. The prompt neutron spectrum is a Maxwellian,  $\chi(E)$ , in energy as reported in formula 1.2 ( $\bar{E} = 2$  MeV) as shown in figure 1.8, in the case of  $^{235}\text{U}$

$$\chi(E) = 0.4537e^{-1.036E} \sinh\sqrt{2.29E} \quad (1.2)$$

The mean number of prompt neutrons emitted in a fission reaction is expressed by equation 1.3

$$\nu(E) = \nu_0 + \alpha E \quad (1.3)$$

where  $\nu_0$  and  $\alpha$  are constants that depend upon the type on nuclei as shown in table 1.2

Nuclide	$\nu_0$	$\alpha$ (MeV <sup>-1</sup> )	Energy range (MeV)
Th <sup>232</sup>	1.87	0.164	all energy
<sup>233</sup> U	2.48	0.075	E ≤ 1
	2.41	0.136	E > 1
<sup>235</sup> U	2.43	0.065	E ≤ 1
	2.35	0.150	E > 1
<sup>238</sup> U	2.30	0.160	all energies
<sup>239</sup> Pu	2.87	0.148	E ≤ 1
	2.91	0.133	E > 1

Table 1.2:  $\nu_0$  and  $\alpha$  values for different nuclides

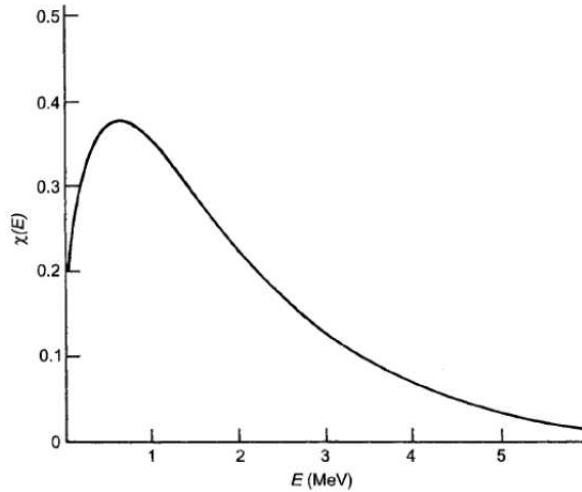


Figure 1.8: Energy distribution of prompt neutrons

As said in the previous paragraph, during fission reactions prompt and delayed neutrons (less than 1% of the total neutrons) are emitted. Delayed neutrons are fundamental in order to guarantee safety operation conditions in a nuclear reactor and are created in the decay by neutron emission of nuclei produced following the  $\beta^-$  decay of some fission fragments. For example, <sup>87</sup>Br decays  $\beta^-$  with half life 55.65 s in the ground state or excited state (about

5.4 MeV) of  $^{87}\text{Kr}$  (figure 1.9) which contains 51 neutrons, just one more than the magic number 50, with binding energy of 5.1 MeV. When we are in the excited state of  $^{87}\text{Kr}$ , the excitation energy is sufficient for a neutron emission. Nuclei like  $^{87}\text{Kr}$  are called delayed neutron precursors, which are divided into six groups according to their mean half lives ( $\lambda_i$ ) as reported in table 1.3. ( $\beta_i$  is the fraction of delayed neutrons with respect to the total number of emitted neutrons in each group)

Group	$T_{1/2}(s)$	$\lambda_i (s^{-1})$	Fraction ( $\beta_i$ )
1	55.72	0.0124	0.000215
2	22.72	0.0305	0.001424
3	6.22	0.111	0.001274
4	2.3	0.301	0.002568
5	0.61	1.24	0.000748
6	0.23	3.01	0.000273

Table 1.3: Characteristics of delayed neutron precursors

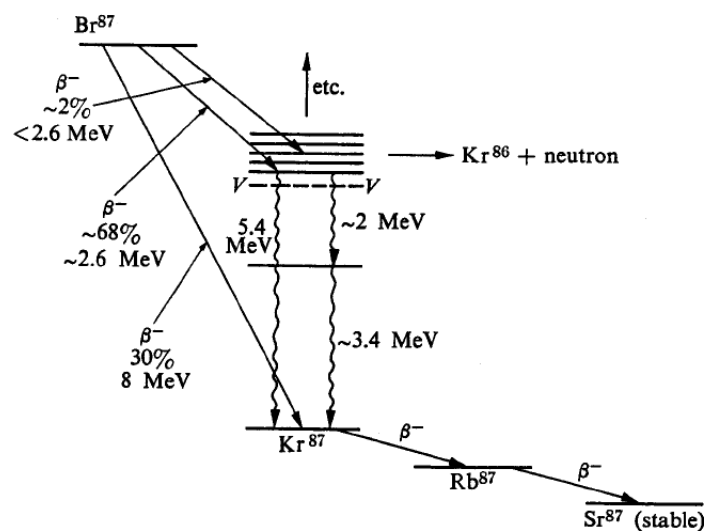


Figure 1.9: Origin of delayed neutron from  $^{87}\text{Kr}$

## 1.2.2 Chain reaction and multiplication factor

Since two or three neutrons are released in every neutron-induced fission reaction, there is the possibility to have a sustained neutron chain reaction. To sustain a fission chain reaction, one or more of the neutrons produced in the fission event must, on average, survive to produce another fission event. There is competition for the fission neutrons in any assembly, i.e. some others will be absorbed in fuel nuclides as radiative capture events rather than fission events, some will be absorbed by non-fuel materials, and some will leak out of the assembly (active core). A scattering event does not compete for a neutron because the scattered neutron remains in the assembly being available for causing a fission event. A scattering event does change a neutron energy and thus, because the various cross sections are energy dependent, does change the relative likelihood of the next interaction being a fission event.

The fission cross sections for the fissile nuclides increase approximately as  $1/v$  (where  $v$  is the speed of neutron) with decreasing neutron energy, but then so do the capture cross sections of the fissile nuclides. The probability that a neutron absorbed in a fissile nuclide causes a fission is

$$\frac{\sigma_f}{\sigma_a} = \frac{\sigma_f}{\sigma_c + \sigma_f} = \frac{1}{1 + \frac{\sigma_c}{\sigma_f}} = \frac{1}{1 + \alpha} \quad (1.4)$$

where  $\alpha$  is the capture-to-fission ratio. The capture-to-fission ratio for the principal fissile nuclides decreases as the neutron energy increases. For high neutron energies, the fission probability, which varies as reported in (1.4), is larger for  $^{239}\text{Pu}$  than for  $^{235}\text{U}$  and  $^{233}\text{U}$ , but the situation is reversed for thermal neutrons.

The product of the fission probability for a neutron absorbed in the fuel with the average number of neutrons released per fission given by

$$\eta = \nu \frac{\sigma_f}{\sigma_c + \sigma_f} = \frac{\nu}{1 + \alpha} \quad (1.5)$$

This quantity provides a better characterization of the capabilities of the different fissile nuclides to sustain a fission chain reaction and is plotted in figure 1.10 for the principal fissile nuclides. For high neutron energies,  $\eta$  is higher for  $^{239}\text{Pu}$  than for  $^{235}\text{U}$  and  $^{233}\text{U}$ , but the situation is reversed for thermal neutrons.

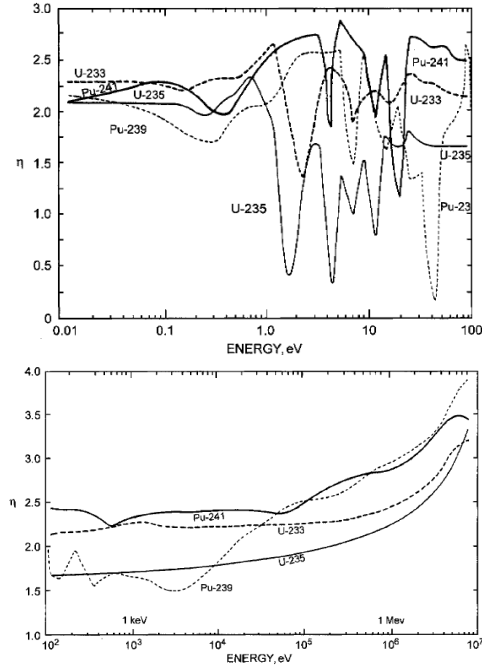


Figure 1.10:  $\eta$  for principal fissile nuclides in the low (upper panel) and high (lower panel) energy regions

### 1.2.3 Neutron utilization factor

The utilization factor is defined as the fraction out of total neutrons which are absorbed in fissile materials

$$f = \frac{N^{fiss} \sigma_a^{fiss}}{N^{fiss} \sigma_a^{fiss} + N^{other} \sigma_a^{other}} \quad (1.6)$$

Since the absorption cross section,  $\sigma_a = \sigma_f + \sigma_c$ , is much greater for thermal neutrons than for fast neutrons in the case of fissile nuclides, but comparable for fast and thermal neutrons in the case of non-fissile fuel nuclides and structural nuclides, so the utilization factor for a given composition is much greater for thermal neutrons than for fast neutrons (and, in fact, is usually referred to as the thermal utilization factor).

### 1.2.4 Fast fission

The product  $\eta f$  is the number of neutrons produced by fissile nuclides per each neutron absorbed. There will also be neutrons produced by the fission of the non-fissile fuel nuclides, mostly by fast neutrons. The fast fission factor  $\epsilon$  is the total fission neutron production rate/fission neutron production rate in fissile nuclides, the quantity  $\eta f \epsilon$  is the total number of fission neutrons produced for each neutron absorbed in the assembly. The total number of fission neutrons produced, on average, per each neutron introduced into the assembly by a previous fission event is  $\eta f \epsilon P_{NL}$ , where  $P_{NL}$  is the non leakage probability.

### 1.2.5 Effective multiplication factor

The effective multiplication factor is defined by the following equation

$$k_{eff} = \eta f \epsilon p P_{NF} = k_{\infty} P_{NF} \quad (1.7)$$

where  $p$  is the escape probability from  $^{238}\text{U}$  resonances and  $P_{NF}$  is the non escape probability from reactor core volume. This factor has a fundamental role in reactor physics: it represents the ratio between the number of neutrons in a generation and the previous one. In the critical condition  $k_{eff}=1$ , the neutron population in the assembly will remain constant in the sub-critical condition  $k_{eff}<1$  the neutron population in the assembly will decrease. If more than one fission neutron survives to induce another fission event the neutron population in the assembly will increase: this condition is called super-critical  $k_{eff}>1$ . The effective multiplication factor depends on the composition ( $k_{\infty}$ ) and size ( $P_{NL}$ ) of an assembly.

### 1.2.6 Reactor kinetics

If  $N(t)$  represents the number of fission neutrons introduced into an assembly at the instant  $t$ , and if  $l$  is the average time required for a fission neutron to slow down and be absorbed or leak out, the number of neutrons at time  $t+C$  is equal to

$$N(t + C) = k_{eff} N(t) \quad (1.8)$$

This relation describes the reactor kinetics and typical values of  $C$  are of the order of  $10^{-4}$  s for an assembly with thermal neutrons. If we consider  $t \ll C$ , it is possible to write the first member of 1.8 in Taylor series and taking into account only the first term in the expansion, we get

$$N(t) + \frac{dN(t)}{dt}C = k_{eff}N(t) \quad (1.9)$$

and considering the source contribution to neutron population

$$\frac{dN(t)}{dt} = \frac{k_{eff} - 1}{C}N(t) + S(t) \quad (1.10)$$

The solution of 1.10 is given by

$$N(t) = N_0 e^{\left(\frac{k_{eff}-1}{C}t\right)} + \frac{SC}{k_{eff} - 1} \left( e^{\left(\frac{k_{eff}-1}{C}t\right)} - 1 \right) \quad (1.11)$$

This equation has, for  $k < 1$ , an asymptotic ( $t \gg 1$ ) solution

$$N(t) = \frac{SC}{1 - k_{eff}} \quad (1.12)$$

In this case the reactor is subcritical, then the chain reaction is not self-sustained: in fact there is the contribution of the source, necessary to maintain operative the reactor.

The reactor period is defined as

$$T = \frac{C}{k_{eff} - 1} \quad (1.13)$$

and represents the variation of neutron population by a factor of "e" (e-folding time).

The neutron cycle  $C_d$ , considering the delayed neutrons contribution, is defined as

$$C_d = (1 - \beta)C + \sum_{i=1}^6 \beta_i C_i \quad (1.14)$$

where  $\beta_i$  are the fractions of delayed neutrons for each of  $i$ -th group ( $i=1-6$ ) and beta is defined as the summation of the  $\beta_i$ . In this case  $C$  is greater with

respect to the case with only prompt neutrons allowing the control of reactor in a case of  $k_{eff}$  variation.

Another important parameter is the reactivity, defined as

$$\rho = \frac{k_{eff} - 1}{k_{eff}} \quad (1.15)$$

and is commonly measured in dollars [\$], where 1 \$ is defined by the relation  $1\$ = \beta$ , with  $\beta$  fraction of delayed neutrons.

### 1.2.7 Neutron flux

Neutron flux is defined as

$$\phi(\mathbf{r}) = vn(\mathbf{r}) \quad (1.16)$$

where  $v$  is the neutrons speed and  $n(\mathbf{r})$  is the neutron density at the point  $\mathbf{r}$ . The neutron flux defined this way represents the total path of neutrons in a volume around  $\mathbf{r}$  in a second.

It is useful the definition of the effective cross section

$$\sigma_{eff} = \frac{\int_{E_{min}}^{E_{max}} \sigma_f(E)\phi(E)dE}{\int_{E_{min}}^{E_{max}} \phi(E)dE} \quad (1.17)$$

which represents the reaction cross section weighted on the reactor flux spectrum.

## 1.3 Thermal and fast reactors

One of the possible reactors classification is based on the presence of a moderator, able to bring the fission neutron energy to thermal regions.

### 1.3.1 Thermal reactors

$^{235}\text{U}$  and  $^{239}\text{Pu}$  fission cross sections, as shown in the previous paragraph, increase decreasing neutrons kinetic energy, it is useful to get neutron slowing

down by using, for instance, water, heavy water or graphite in order to increase the fission reaction rate defined as

$$R_f = \int_{E_{min}}^{E_{max}} \sigma_f(E)\phi(E)dE \quad (1.18)$$

Considering an elastic scattering between a neutron (kinetic energy  $E$  and velocity  $v$ ) and a nucleus with atomic mass  $A$  at rest, the ratio between the neutron energy after ( $E'$ ) and before collision considering momentum and energy conservation laws is:

$$\frac{E'}{E} = \frac{1 + A^2 + 2A\cos\theta}{(A + 1)^2} \quad (1.19)$$

where  $\theta$  is the scattering angle in CM system.

The maximum energy loss is for  $\theta=\pi$  and equation 1.19 becomes

$$\frac{E'(min)}{E} = \frac{(A - 1)^2}{(A + 1)^2} = \alpha \quad (1.20)$$

The average energy loss is:

$$\langle \Delta E \rangle = \int_{\alpha E}^E (E - E')P(E \rightarrow E')dE' = \frac{1 - \alpha}{2}E \quad (1.21)$$

The average logarithmic energy loss is:

$$\xi = \langle \log \frac{E}{E'} \rangle = \int_{\alpha E}^E \log \frac{E}{E'}P(E - E')dE' = 1 - \frac{\alpha}{1 - \alpha} \log \alpha \quad (1.22)$$

Substituting  $\alpha = \frac{(A-1)^2}{(A+1)^2}$  in equation 1.22 we obtain:

$$\xi = 1 + \frac{(A - 1)^2}{2A} \log \frac{(A - 1)}{(A + 1)} \quad (1.23)$$

As we can see, the mean logarithmic decrement is independent of the initial neutron energy  $E$ .

After  $n$  collision the mean logarithmic decrement is:

$$\xi = \frac{1}{n} \log \frac{E}{E'} \quad (1.24)$$

then the number of collisions in order to slow the neutrons from E to E' is:

$$n = \frac{1}{\xi} \log \frac{E}{E'} \quad (1.25)$$

In table 1.4 are reported the values of the number of neutron collisions in order to slowing down the neutron energy to thermal region values.

Material	Collisions
Light water	19
Heavy water	35
Helium	42
Beryllium	86
Boron	105
Carbon	114
Oxygen	150
Uranium	2172

Table 1.4: Number of collisions to thermalize neutrons

The ability of a given material to slow down neutrons is referred to as the macroscopic slowing down power (MP) defined as the product of the logarithmic energy decrement per collision and the macroscopic neutron scattering cross section as follows:

$$MP = \xi \Sigma_s$$

Macroscopic slowing down power indicates how rapidly slowing down occurs in the material in question, but it does not completely define the moderation effectiveness of the material. An element such as boron has a high logarithmic energy decrement and a good slowing down power, but is not a good moderator because of its high absorption cross section, and may be accounted for by dividing the macroscopic slowing down power by the macroscopic absorption cross section. This relationship is called the moderating ratio (MR) given by:

$$MR = \frac{\xi \Sigma_s}{\Sigma_a}$$

Mean logarithmic decrement ( $\xi$ ), macroscopic slowing down power and moderating ratio values for different materials are reported in table 1.5.

Material	$\xi$	MP	MR
Light water	0.927	1.425	62
Heavy water	0.510	0.177	4830
Helium	0.427	$9 \times 10^{-6}$	51
Beryllium	0.207	0.154	126
Boron	0.171	0.092	$6.6 \times 10^{-4}$
Carbon	0.158	0.083	216

Table 1.5: Mean logarithmic decrement ( $\xi$ ) macroscopic slowing down power (MP) and moderating ratio (MR) values for different materials

### 1.3.2 Fast reactors

Unlike thermal, fast reactors contain no moderator: they are substantially composed by an assembly of fuel with a coolant without moderation properties, for example solid or liquid lead [5]. Neutron spectrum covers the epithermal and fast energetic regions. The great advantage of fast spectra consists in the induction of fission reactions for the great part of minor actinides nuclides (Np, Cm, Am). As we can see in figure 1.11, fast neutrons give an important contribution to burn minor actinides which represents a little percentage of nuclear waste, but they are the more radiotoxic part. A drawback with respect to thermal reactors is the need of larger quantity of fissile material because of the lower fission cross section in these energetic regions and therefore a fission rate decreasing.

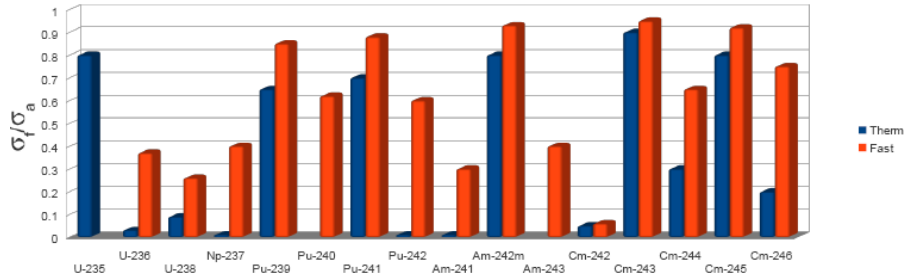


Figure 1.11: Contribution of fast neutrons to minor actinides fission

Another important feature of fast neutron spectrum is the possibility of transmute some fission fragments having long half-life. For example lead material, as coolant, is indeed able to shift the neutron energy down into the resonance region for capture cross section of fission products as shown in figure 1.12.

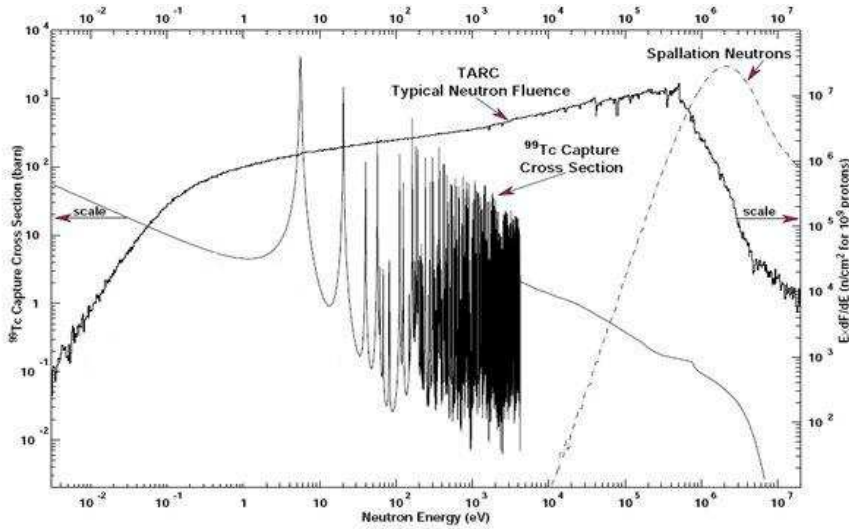


Figure 1.12: Transmutation of fission fragments with fast neutron spectrum

The spent fuel relative radiotoxicity (defined as the product between a dose factor and the activity of a nuclide  $R(Sv)=F_d(Sv/Bq)\times A(Bq)$ ) as a function of time is show in figure 1.13, where the green line represents the

relative fuel radiotoxicity with direct disposal (fission products+minor actinides+Plutonium), the light blue line represents the fuel relative radiotoxicity considering the Plutonium recycle and the blue line represents the fuel relative radiotoxicity considering Plutonium recycle the partitioning and transmutation of minor actinides as in the case of fast reactors. As one can see, the relative radiotoxicity (blue line) is lower than the radiotoxicity in the others cases.

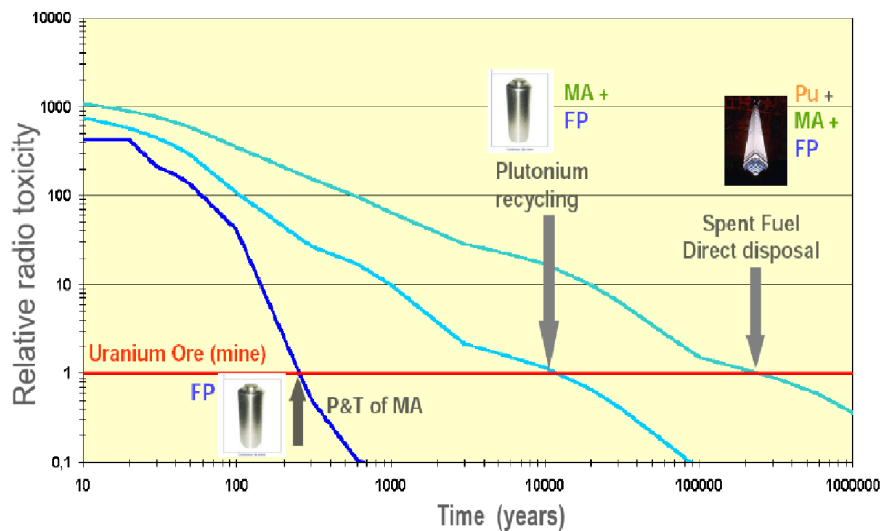


Figure 1.13: Relative radiotoxicity of spent fuel as a function of time



# Chapter 2

## Fuel burn-up calculations and measurements

### 2.1 Fuel burn-up

The long-term changes in the properties of a nuclear reactor over its lifetime are determined by the changes in fuel composition due to burn-up and the way how these are compensated [6]. The fuel management is strongly affected by the efficiency of fuel utilization to produce power, which in turn is affected by these long-term changes associated with fuel burn-up. In this chapter we describe the changes in fuel composition that take place in an operating reactor as well as their effects on the reactor. The effects of the Samarium and Xenon fission products with large thermal neutron absorption cross sections. Moreover the breeding of fertile material obtained to fissionable material by neutron transmutation.

Fuel from natural Uranium contain a mixture of  $^{234}\text{U}$ ,  $^{235}\text{U}$  and  $^{238}\text{U}$ : the fraction of fissile nuclide can vary from 0.72% (natural Uranium) to 90% (High Enriched Uranium).

During the operation of a nuclear reactor a number of changes occur in the fuel composition. The various nuclei are transmuted by neutron capture and subsequent decay. For a uranium-fueled reactor, this process produces a variety of transuranic elements in particular some actinides (Np, Pu, Am, Cm). For

a Thorium-fueled reactor, a number of Uranium isotopes are produced. The fission process destroys a fissile nucleus producing lighter nuclei called fission products. Fission products tend to be neutron-rich and decay by beta or neutron emission (usually accompanied by gamma emission) [7].

### 2.1.1 Bateman equations

The time variation of concentrations for the various fuel isotopes in a reactor are described by a coupled set of equations

$$\begin{cases} \frac{dN^{U^{235}}(t)}{dt} = -(\lambda^{U^{235}} + \sigma_a^{U^{235}} \phi) N^{U^{235}}(t) \\ \frac{dN^{FP}(t)}{dt} = Y^{FP} \sigma_f^{U^{235}} \phi N^{U^{235}}(t) - (\lambda^{FP} + \sigma_a^{FP} \phi) N^{FP}(t) \end{cases}$$

where  $Y$  is the fission yield,  $\lambda$  is the decay constant,  $\sigma_a$  and  $\sigma_f$  are the fission and absorption cross sections respectively.

This kind of coupled systems represents the time evolution of  $^{235}\text{U}$  and  $^{238}\text{U}$  nuclei. The first term of the first equation accounts for the disappearance term (decay and neutron absorption), while the second equation is the evolution of fission products from  $^{235}\text{U}$  fission.

$$\begin{cases} \frac{dN^{U^{238}}(t)}{dt} = -(\lambda^{U^{238}} + \sigma_a^{U^{238}} \phi) N^{U^{238}}(t) \\ \frac{dN^{U^{239}}(t)}{dt} = \sigma_{n,\gamma}^{U^{238}} \phi N^{U^{238}}(t) - (\lambda^{U^{239}} + \sigma_a^{U^{239}} \phi) N^{U^{239}}(t) \\ \frac{dN^{Np^{239}}(t)}{dt} = \lambda^{U^{239}} N^{U^{239}}(t) - (\lambda^{Np^{239}} + \sigma_a^{Np^{239}} \phi) N^{Np^{239}}(t) \\ \frac{dN^{Pu^{239}}(t)}{dt} = \lambda^{Np^{239}} N^{Np^{239}}(t) - (\lambda^{Pu^{239}} + \sigma_a^{Pu^{239}} \phi) N^{Pu^{239}}(t) \end{cases}$$

This system represents the evolution of  $^{238}\text{U}$  which forms  $^{239}\text{Pu}$  by a neutron capture and two subsequent  $\beta^-$  decay, The first term of each equation is the appearance term (neutron capture or decay) while the second is the disappearance term (neutron absorption and decay).

The solution of this differential equations systems for  $^{235}\text{U}$  is:

$$N^{U^{235}}(t) = N_0^{U^{235}} e^{-(\lambda^{U^{235}} + \sigma_a^{U^{235}} \phi)t}$$

while for fission products we have

$$N^{FP}(t) = \frac{Y^{FP} \sigma_f^{U^{235}} \phi N_0^{U^{235}}}{\lambda^{FP} - \lambda^{U^{235}} + (\sigma_a^{FP} - \sigma_a^{U^{235}}) \phi} \left( e^{-(\lambda^{U^{235}} + \sigma_a^{U^{235}} \phi)t} - e^{-(\lambda^{FP} + \sigma_f^{FP} \phi)t} \right)$$

for  $^{238}\text{U}$

$$N^{U^{238}}(t) = N_0^{U^{238}} e^{-(\lambda^{U^{238}} + \sigma_a^{U^{238}} \phi)t}$$

for  $^{239}\text{U}$

$$N^{U^{239}}(t) = \frac{N_0^{U^{238}} \sigma_{n,\gamma}^{U^{238}} \phi}{\lambda^{U^{239}} - \lambda^{U^{238}} + (\sigma_a^{U^{239}} - \sigma_a^{U^{238}}) \phi} \left( e^{-(\lambda^{U^{238}} + \sigma_a^{U^{238}} \phi)t} - e^{-(\lambda^{U^{239}} + \sigma_a^{U^{239}} \phi)t} \right)$$

for  $^{239}\text{Np}$

$$N^{Np^{239}}(t) = \frac{N_0^{U^{238}} \sigma_{n,\gamma}^{U^{238}} \phi \lambda^{U^{239}}}{\lambda^{U^{239}} - \lambda^{U^{238}} + (\sigma_a^{U^{239}} - \sigma_a^{U^{238}}) \phi} \left( \frac{e^{-(\lambda^{U^{238}} + \sigma_a^{U^{238}} \phi)t}}{\lambda^{Np^{239}} - \lambda^{U^{238}} + (\sigma_a^{Np^{239}} - \sigma_a^{U^{238}}) \phi} + \right. \\ \left. - \frac{e^{-(\lambda^{U^{239}} + \sigma_a^{U^{239}} \phi)t}}{\lambda^{Np^{239}} - \lambda^{U^{239}} + (\sigma_a^{Np^{239}} - \sigma_a^{U^{239}}) \phi} + \right. \\ \left. + \left( \frac{e^{-(\lambda^{Np^{239}} + \sigma_a^{Np^{239}} \phi)t}}{\lambda^{Np^{239}} - \lambda^{U^{239}} + (\sigma_a^{Np^{239}} - \sigma_a^{U^{239}}) \phi} - \frac{e^{-(\lambda^{Np^{239}} + \sigma_a^{Np^{239}} \phi)t}}{\lambda^{Np^{239}} - \lambda^{U^{238}} + (\sigma_a^{Np^{239}} - \sigma_a^{U^{238}}) \phi} \right) \right)$$

and for  $^{239}\text{Pu}$

$$N^{Pu^{239}}(t) = \frac{N_0^{U^{238}} \sigma_{n,\gamma}^{U^{238}} \phi \lambda^{U^{239}} \lambda^{Np^{239}}}{\lambda^{U^{239}} - \lambda^{U^{238}} + (\sigma_a^{U^{239}} - \sigma_a^{U^{238}}) \phi} \\ \left( \left( \frac{1}{\lambda^{Np^{239}} - \lambda^{U^{238}} + (\sigma_a^{Np^{239}} - \sigma_a^{U^{238}}) \phi} \right) \left( \frac{e^{-(\lambda^{U^{238}} + \sigma_a^{U^{238}} \phi)t}}{\lambda^{Pu^{239}} - \lambda^{U^{238}} + (\sigma_a^{Pu^{239}} - \sigma_a^{U^{238}}) \phi} \right) + \right.$$

$$\begin{aligned}
& - \left( \frac{1}{\lambda_{Np^{239}} - \lambda_{U^{239}} + (\sigma_a^{Np^{239}} - \sigma_a^{U^{239}})\phi} \right) \left( \frac{e^{-(\lambda_{U^{239}} + \sigma_a^{U^{239}})\phi}t}{\lambda_{Pu^{239}} - \lambda_{U^{239}} + (\sigma_a^{Pu^{239}} - \sigma_a^{U^{239}})\phi} \right) + \\
& + \left( \frac{1}{\lambda_{Np^{239}} - \lambda_{U^{239}} + (\sigma_a^{Np^{239}} - \sigma_a^{U^{239}})\phi} - \frac{1}{\lambda_{Np^{239}} - \lambda_{U^{238}} + (\sigma_a^{Np^{239}} - \sigma_a^{U^{238}})\phi} \right) \\
& \quad \left( \frac{e^{-(\lambda_{Np^{239}} + \sigma_a^{Np^{239}})\phi}t}{\lambda_{Pu^{239}} - \lambda_{Np^{239}} + (\sigma_a^{Pu^{239}} - \sigma_a^{Np^{239}})\phi} \right) + \\
& + \left( \frac{1}{\lambda_{Np^{239}} - \lambda_{U^{239}} + (\sigma_a^{Np^{239}} - \sigma_a^{U^{239}})\phi} \frac{1}{\lambda_{Pu^{239}} - \lambda_{U^{239}} + (\sigma_a^{Pu^{239}} - \sigma_a^{U^{239}})\phi} \right) + \\
& - \left( \frac{1}{\lambda_{Np^{239}} - \lambda_{U^{238}} + (\sigma_a^{Np^{239}} - \sigma_a^{U^{238}})\phi} \frac{1}{\lambda_{Pu^{239}} - \lambda_{U^{238}} + (\sigma_a^{Pu^{239}} - \sigma_a^{U^{238}})\phi} \right) + \\
& - \left( \frac{1}{\lambda_{Np^{239}} - \lambda_{U^{239}} + (\sigma_a^{Np^{239}} - \sigma_a^{U^{239}})\phi} - \frac{1}{\lambda_{Np^{239}} - \lambda_{U^{238}} + (\sigma_a^{Np^{239}} - \sigma_a^{U^{238}})\phi} \right) \\
& \quad \left( \frac{1}{\lambda_{Pu^{239}} - \lambda_{Np^{239}} + (\sigma_a^{Pu^{239}} - \sigma_a^{Np^{239}})\phi} \right) e^{-(\lambda_{Pu^{239}} + \sigma_a^{Pu^{239}})\phi}t
\end{aligned}$$

These equations will be used in this work in order to have an analytical description of nuclides concentrations time evolution for the MCB code validation.

### 2.1.2 Burn-up effects in fuel <sup>1</sup>

There are a variety of changes in reactivity effects associated with the change in fuel composition due to burn-up. The fission of fissile nuclei produces two negative reactivity effects; the number of fissile nuclei is reduced and fission products are created, many of which have large neutron absorption cross sections. The transmutation-decay chain of fertile nuclei produces a sequence

---

<sup>1</sup>Burn-up is a measure of how much energy is produced from a nuclear fuel source. It is measured both as the fraction of fuel atoms that underwent fission in %FIMA (fissions per initial metal atom) and as the energy released per mass of initial fuel in megawatt-days per ton (MWd/ton).

of actinides (Uranium-fueled reactor) or Uranium isotopes (Thorium-fueled reactor), some of which are fissile. The transmutation of one fertile isotope into another non-fissile isotope can have a positive or negative reactivity effect, depending on the absorption cross sections for the isotopes involved: the transmutation of a fertile isotope into a fissile isotope has a positive reactivity effect.

The reactivity effects of fuel depletion must be compensated to maintain criticality over the fuel burn-up cycle. The major compensating elements are the control rods which are composed for example with boron, with a great absorption cross section and are able to control the reactivity variations.

### 2.1.3 Poisons

The poisons in a reactor are the fission products with a great absorption cross section. The poisons are divided into two groups: saturable poisons ( $^{149}\text{Sm}$  and  $^{135}\text{Xe}$ ) which saturate after days or month reactor operation and non-saturable poisons which are continuously accumulated during the reactor operation [5].

#### Saturable poisons

In this paragraph is reported the behavior of one of the most important saturable poison:  $^{135}\text{Xe}$ .

$^{135}\text{Xe}$  has a thermal absorption cross section of  $2.6 \times 10^6$  b ( $t_{\frac{1}{2}}=9.1$  h) It is produced directly from fission, with yield  $Y^{Xe^{135}}$ , and from the decay of  $^{135}\text{I}$  ( $t_{\frac{1}{2}}=6.6$  h), which in turn is produced by the decay of the direct fission product  $^{135}\text{Te}$  ( $t_{\frac{1}{2}}=19$  s), with yield  $Y^{Te^{135}}$ .

The  $^{135}\text{I}$  and  $^{135}\text{Xe}$  production rates are:

$$\frac{dN^{I^{135}}(t)}{dt} = Y^{Te^{135}} \sigma_f \phi N^{U^{235}}(t) - \lambda^{I^{135}} N^{I^{135}}(t) \quad (2.1)$$

$$\frac{dN^{Xe^{135}}(t)}{dt} = Y^{Xe^{135}} \sigma_f \phi N^{U^{235}}(t) + \lambda^{I^{135}} N^{I^{135}}(t) - (\lambda^{Xe^{135}} + \sigma_a^{Xe^{135}} \phi) N^{Xe^{135}}(t) \quad (2.2)$$

The solution of equation 2.1 is

$$N^{I^{135}}(t) = \frac{Y^{Te^{135}} \sigma_f \phi}{\lambda^{I^{135}} N_0^{U^{235}}} (1 - e^{-\lambda^{I^{135}} t}) + N_0^{I^{135}} e^{-\lambda^{I^{135}} t} \quad (2.3)$$

while the solution of equation 2.2 is:

$$N^{Xe^{135}}(t) = \frac{(Y^{Te^{135}} + Y^{Xe^{135}}) N_0^{U^{235}}}{\lambda^{Xe^{135}} + \sigma_a^{Xe^{135}} \phi} (1 - e^{-(\lambda^{Xe^{135}} + \sigma_a^{Xe^{135}} \phi)t}) + \quad (2.4)$$

$$+ \frac{\lambda^{Te^{135}} - \lambda^{I^{135}} N^{I^{135}}}{\lambda^{Xe^{135}} - \lambda^{I^{135}} + \sigma_a^{Xe^{135}} \phi} (e^{-(\lambda^{Xe^{135}} + \sigma_a^{Xe^{135}} \phi)t} - e^{-\lambda^{I^{135}} t}) + N_0^{Xe^{135}} e^{-(\lambda^{Xe^{135}} + \sigma_a^{Xe^{135}} \phi)t}$$

The equilibrium population, which is obtained by setting  $\frac{dN^{Xe^{135}}(t)}{dt} = 0$ , is respectively for  $^{135}\text{I}$  and for  $^{135}\text{Xe}$  is

$$N_{eq}^{I^{135}} = \frac{Y^{Te^{135}} \sigma_f \phi}{\lambda^{I^{135}}} \quad (2.5)$$

$$N_{eq}^{Xe^{135}} = \frac{(Y^{Xe^{135}} + Y^{Te^{135}}) \sigma_f \phi}{\lambda^{Xe^{135}} + \sigma_a^{Xe^{135}} \phi} \quad (2.6)$$

When a reactor is shut down from an equilibrium Xenon condition, the Iodine and Xenon populations satisfy equations 2.3 and 2.4 considering  $N^{I^{135}}(0) = N_{eq}^{I^{135}}$  and  $N^{Xe^{135}}(0) = N_{eq}^{Xe^{135}}$  and  $\phi = 0$

$$N^{I^{135}}(t) = N_{eq}^{I^{135}} e^{-\lambda^{I^{135}} t} \quad (2.7)$$

$$N^{Xe^{135}}(t) = N_{eq}^{Xe^{135}} e^{-\lambda^{Xe^{135}} t} + N_{eq}^{I^{135}} \frac{\lambda^{I^{135}}}{\lambda^{I^{135}} - \lambda^{Xe^{135}}} (e^{-\lambda^{I^{135}} t} - e^{-\lambda^{Xe^{135}} t}) \quad (2.8)$$

If  $\phi > \frac{Y^{Xe^{135}} \lambda^{Xe^{135}}}{Y^{I^{135}} \sigma_a^{Xe^{135}}}$ , the Xenon concentration will be build-up after shut-down to a peak value as shown in fig 2.1 and then decays to zero.

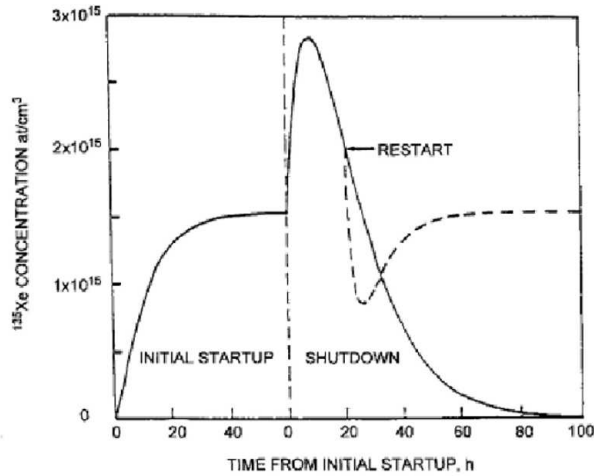
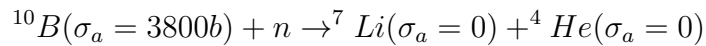


Figure 2.1:  $^{135}\text{Xe}$  concentration during start-up, shutdown and restart periods

If the reactor is restarted before the Xenon has entirely decayed, the Xenon concentration will initially decrease because of the burnout of Xenon and then gradually build up again because of the decay of a growing Iodine concentration, returning to values of  $N_{eq}^{I^{135}}$  and  $N_{eq}^{Xe^{135}}$  for the new power level.

### Burnable poisons

Burnable poisons are inserted in the fuel in order to compensate the negative reactivity effects: they are characterized by an high value of the absorption cross section. They compensate the negative reactivity effects absorbing a neutron and decaying into an isotope with a lower value of absorption cross section



### Non-saturable poisons

Non-saturable poisons come from fission process and have a smaller neutron absorption cross section than saturable poisons, in particular Samarium and Xenon, for this reason it is not possible a saturation of this kind of nuclides.

From literature [30] the complete assembly of non-saturable poisons can be considered as a lumped fission product with neutron absorption cross section of about 50 b per fission (25 b each fission fragment). The concept of lump fission product will be used in the simulations described in section 3.4.

## 2.2 Fuel burn-up calculation codes

MCB [8] is a Monte Carlo Continuous Energy Burnup Code for a general-purpose use for the calculation of the time evolution of nuclides with burn-up or decay. It includes eigenvalue calculations of critical and sub-critical systems as well as neutron transport calculations in fixed source mode or k-code (for critical systems) mode to obtain reaction rates and energy deposition that are necessary for burn-up calculations. MCB is compatible with MCNP [20] and preserves its input file structure of it. Complete burn-up calculations can be performed in a one single run and it requires preparation of only one input file by a little modification of an MCNP input file. The code was extensively tested in benchmark calculations and reactor core design [31].

The core of this code is the density nuclide calculation based on the Bateman equations solutions representing the time evolution of nuclide density.

There are some other burn-up calculation codes, as ORIGEN. This is a deterministic code, but it is modeled on power reactors, so for our purpose it is non useful because it is not so flexible in the determination of effective cross sections and core geometry.

Instead it is possible to design with MCB a precise geometric core structure and a source: the effective cross sections are calculated using the real fuel element neutron spectrum obtained considering materials and geometry definition.

## 2.3 MCB code: experimental validation

MCB code has been both analytically and experimentally validated. The analytical validation, as explained in the following paragraph, has been obtained by a comparison between the MCB output and analytic formulas results.

### 2.3.1 MCB analytical validation

In this section are reported the results of MCB analytical validation. Two irradiation simulations of natural Uranium and Thorium targets have been performed in order to compare this code outputs with the analytical Bateman equations results [9].

The simulation characteristics are:

- Materials: natural Uranium (99.28%  $^{238}\text{U}$ , 0.72%  $^{235}\text{U}$ ) and natural Thorium (100%  $^{232}\text{Th}$ )
- Uranium target geometry: a cylinder of mass 0.3889 g, radius  $r=0.635$  cm and thickness  $s=0.0161$  cm (figure 2.2)
- Thorium target geometry: a cylinder of mass 0.1412 g, radius  $r=0.635$  cm and thickness  $s=0.0095$  cm
- Neutron source on a sphere of arbitrary radius ( $R=2$  cm) with constant integral flux value inside the sphere surface *Inward cosine*
- Neutron energy  $E=0.025$  eV (thermal energy) in order to use  $\sigma_{therm}$  cross sections
- Irradiation time  $t=3$  h

In order to estimate auto-absorption phenomena the targets have been density diluted by a factor  $10^6$  and  $10^3$  for Uranium and Thorium respectively.

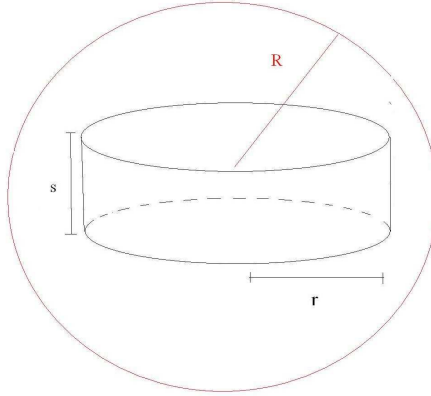


Figure 2.2: Uranium (Thorium) target and irradiation geometry (not to scale)

In table 2.1 are reported the ratios between fission fragments masses:  $M(g)$  from Bateman equations and  $M_{MCB}(g)$  for MCB code.

Isotope	$\frac{M}{M_{MCB}}$	$\frac{M_{MCB}-M}{M_{MCB}} (\%)$
$^{81}\text{Br}$	0.9976	+0.24
$^{90}\text{Sr}$	0.9618	+3.82
$^{99}\text{Mo}$	1.0450	-4.5
$^{99}\text{Tc}$	1.0616	-6.161
$^{132}\text{Te}$	0.9186	+8.13
$^{136}\text{Xe}$	1.1461	-14.61
$^{137}\text{Sb}$	0.8892	+11.08
$^{137}\text{Cs}$	1.0254	-2.54
$^{140}\text{Ba}$	0.9950	+0.49
$^{144}\text{Ce}$	0.8676	+13.23

Table 2.1: Mass values of fission products (Uranium target): in the second column is shown the ration between nuclides masses values calculated using analytical formulas and obtained from MCB code output, in the third column is reported the percentage difference between nuclides masses with analytical formulas and using MCB code)

In table 2.2 are reported the ratios between Actinides masses from Bateman equations and from MCB output.

Isotope	$\frac{M}{M_{MCB}}$	$\frac{M_{MCB}-M}{M_{MCB}}(\%)$
$^{232}\text{Th}$	1	-
$^{233}\text{Th}$	0.9780	+2.20
$^{233}\text{Pa}$	1.0031	-0.31
$^{233}\text{U}$	1.0332	-3.32
$^{235}\text{U}$	1	-
$^{238}\text{U}$	1	-
$^{239}\text{U}$	0.9974	+0.25
$^{239}\text{Np}$	0.9985	+0.15
$^{239}\text{Pu}$	1.0032	-0.32

Table 2.2: Mass values of Actinides (Uranium and Thorium targets): in the second column is shown the ration between nuclides masses values calculated using analytical formulas and obtained from MCB code output, in the third column is reported the percentage difference between nuclides masses with analytical formulas and using MCB code)

### 2.3.2 MCB experimental validation

The experimental validation has been performed by comparing the activity results from MCB code and from the activities obtained with the irradiation of Uranium and Thorium foils in the Central channel of TRIGA Mark II reactor (chapter 3) and in channels A and B of the sub-critical multiplying complex (chapter 4) of the University of Pavia.

The irradiation characteristics for the Central channel of TRIGA reactor are reported below:

- The reactor power has been fixed at 250 W
- The integral flux is  $(2.16 \pm 0.22) \times 10^{10} \text{ n cm}^{-2} \text{ s}^{-1}$
- Irradiation time: 6 h

- Targets geometry and dimensions are basically as equal as reported in the previous paragraph
- Total neutron fluence:  $(4.67 \pm 0.47) \times 10^{14} \text{ n cm}^{-2}$

The irradiation characteristics for channels A and B of SM1 sub-critical complex are the following:

- The integral flux is  $(5.74 \pm 0.3) \times 10^4 \text{ n cm}^{-2} \text{ s}^{-1}$  (channel A) and  $(2.59 \pm 0.13) \times 10^4 \text{ n cm}^{-2} \text{ s}^{-1}$  (channel B)
- Irradiation time: 341 h
- Uranium target geometry: a cylinder of mass 0.3923 g, radius 0.635 cm and thickness 0.0162 cm
- Thorium target geometry: a cylinder of mass 0.1299 g, radius 0.635 cm and thickness 0.0085 cm
- Total neutron fluence:  $(6.7 \pm 0.34) \times 10^{10} \text{ n cm}^{-2}$  (channel A) and  $(3.2 \pm 0.16) \times 10^{10} \text{ n cm}^{-2}$  (channel B)

The masses of Uranium and Thorium foils were measured with an analytical balance, while the gamma spectra were collected and analyzed by gamma spectrometry using a HPGe detector coupled with GammaVision (TM) tool as shown in figure 2.3

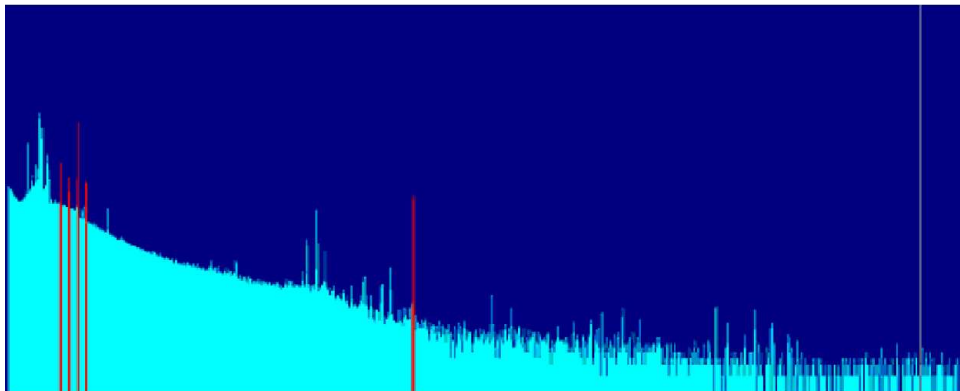


Figure 2.3: Gamma spectrum of one Uranium target before the irradiation

The set of four red peaks in the low energy region of the spectrum represents the  $^{235}\text{U}$  gammas (gamma energy 143.8 keV, 163.4 keV, 185.7 keV and 205.3 keV, while the isolated one is the  $^{234m}\text{Pa}$  photo-peak (gamma energy 1001 keV) in secular equilibrium with  $^{238}\text{U}$ .

The measured Natural Uranium targets masses are

$$m_U = 0.3892 \pm 0.0002g$$

$$m_U = 0.3923 \pm 0.0002g$$

The spectrum for Thorium target is shown in figure 2.4

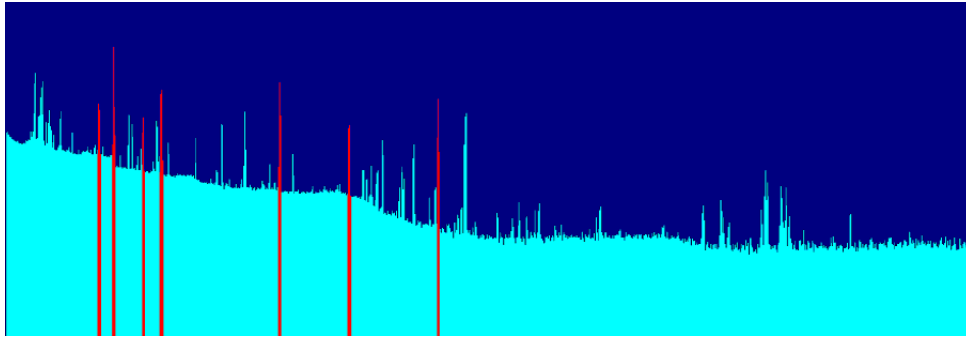


Figure 2.4: Gamma spectrum of one Thorium target before the irradiation

In order to determine the targets masses in figure 2.4 one has to measure the  $^{228}\text{Ra}$  activity (in secular equilibrium with  $^{232}\text{Th}$ ) from  $^{228}\text{Ac}$  (911 keV and 969 keV), and the  $^{228}\text{Th}$  activity from  $^{212}\text{Pb}$  (236.6 keV) and  $^{208}\text{Tl}$  (583.1 keV and 860.4 keV) and the  $^{228}\text{Th}$  activity (in secular equilibrium with  $^{232}\text{Th}$ ) activity from  $^{212}\text{Pb}$  (236.6 keV) and from  $^{208}\text{Tl}$  (583.1 keV and 860.4 keV).

In figure 2.5 are shown  $^{238}\text{U}$ ,  $^{235}\text{U}$  and  $^{232}\text{Th}$  decay chains.

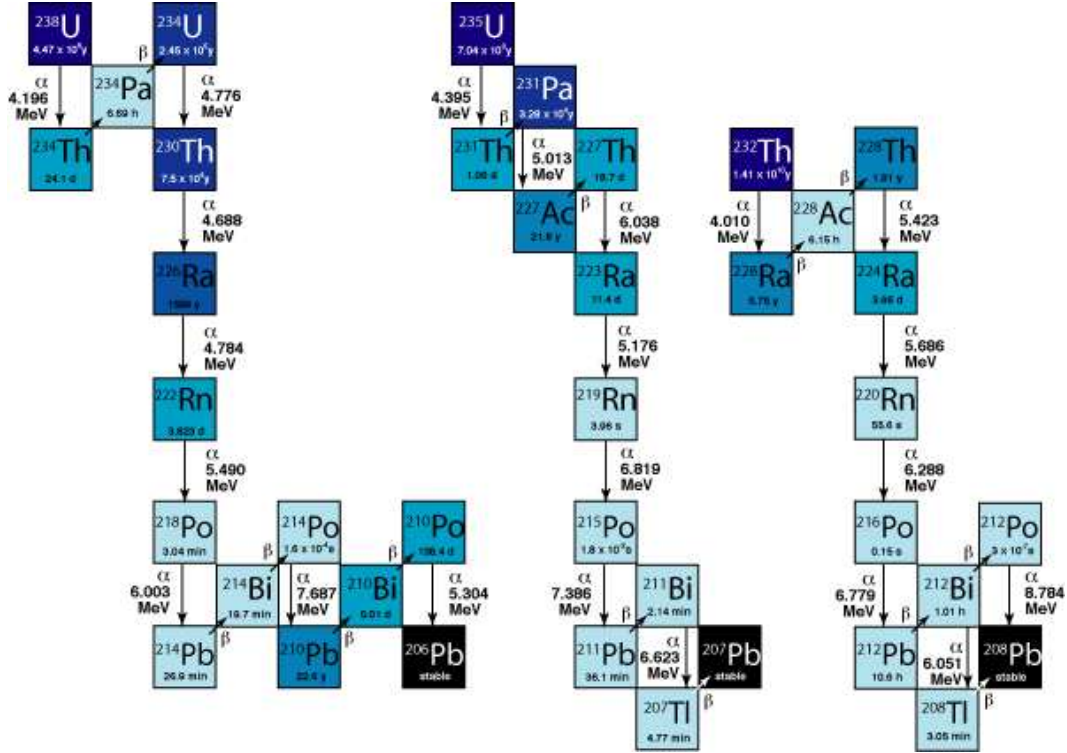


Figure 2.5: <sup>238</sup>U, <sup>235</sup>U and <sup>232</sup>Th decay chains

Since Uranium is a dense material, a fraction of gammas from the different nuclides can be absorbed from target, so it is important to evaluate the attenuation coefficient  $C_{att}$  for different gammas energies. This coefficient has been evaluated using MCNP simulation, considering the Uranium target geometry, and a gammas source uniformly distributed in this volume. The gammas energies are those emitted by the nuclides present in the sample. The original Uranium density ( $19.05 \text{ g/cm}^3$ ) has been diluted by a factor of  $10^6$ , and then the coefficient has been evaluated dividing the gammas flux obtained in the two cases described in detail in section 3.2.2. The values of attenuation coefficient for some gammas energy are shown in table 2.3.

Gamma energy (MeV)	$C_{att}$
0.143	0.649
0.163	0.730
0.186	0.789
0.205	0.824
1	0.987

Table 2.3: Attenuation coefficient as function of gammas energy

The measured Thorium targets masses are

$$m_{Th} = 0.1415 \pm 0.0002g$$

$$m_{Th} = 0.1299 \pm 0.0002g$$

Measured activities of  $^{235}\text{U}$  and  $^{238}\text{U}$  have been compared with the theoretical activities: the results are reported in table 2.4

Nuclide	Theoretical activity (Bq)	Measured activity (Bq)
$^{235}\text{U}$	224.1	224±5
$^{238}\text{U}$	4804.2	4808±105
$^{235}\text{U}$	225.9	223±5
$^{238}\text{U}$	4843.8	4812±105

Table 2.4:  $^{235}\text{U}$  and  $^{238}\text{U}$  theoretical and measured activities

Measured activities of  $^{228}\text{Ra}$  have been compared with the theoretical activities, the results are reported in table 2.5

Nuclide	Theoretical activity (Bq)	Measured activity (Bq)
$^{228}\text{Ra}$	572.8	56812
$^{232}\text{Th}$	572.8	$536 \pm 11$
$^{228}\text{Ra}$	526.5	$505 \pm 10$
$^{232}\text{Th}$	526.5	$474 \pm 9$

Table 2.5:  $^{228}\text{Ra}$  and  $^{232}\text{Th}$  theoretical and measured activities

As one can see, there is a difference between theoretical and measured  $^{232}\text{Th}$  activities which can be attributed to a leakage since  $^{228}\text{Th}$  is gaseous.

Uranium and Thorium targets have been irradiated in the central channel of TRIGA Mark II reactor (chapter 3) and in the sub-critical multiplying complex SM1 of the University of Pavia (U in ring 2 and Th in ring 4) in order to have two different neutron spectra.

### Irradiation at TRIGA Mark II reactor

The top view of TRIGA reactor is shown in figure 2.6, the values of the integral flux in three energy group is reported in table 2.6 [10].

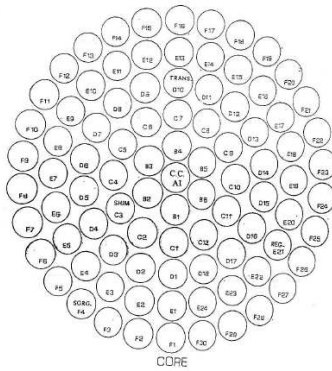


Figure 2.6: Top view of TRIGA reactor core

Energy region	Energy intervals (MeV)	Integral flux ( $n\text{ cm}^{-2}s^{-1}$ )
Thermal	$E \leq 0.55 \times 10^{-6}$	$(7.26 \pm 0.73) \times 10^9$
Epithermal	$0.55 \times 10^{-6} < E \leq 0.1$	$(7.52 \pm 0.75) \times 10^9$
Fast	$E > 0.1$	$(6.78 \pm 0.68) \times 10^9$

Table 2.6: TRIGA Mark II reactor integral flux composition

The integral Central channel TRIGA flux percentages with respect to the total integral flux in the three energy groups is shown in figure 2.7. The integral of flux spectrum is basically shared among the different energy ranges selected.

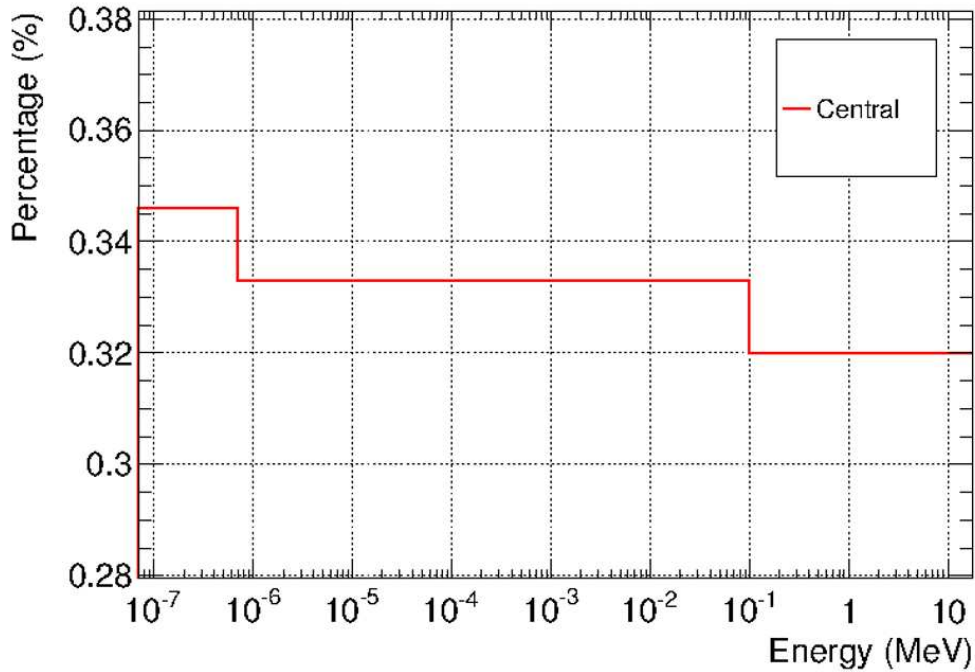


Figure 2.7: Three groups Central channel integral flux percentages

In figure 2.8 the gamma spectrum of irradiated Uranium target is also plotted.

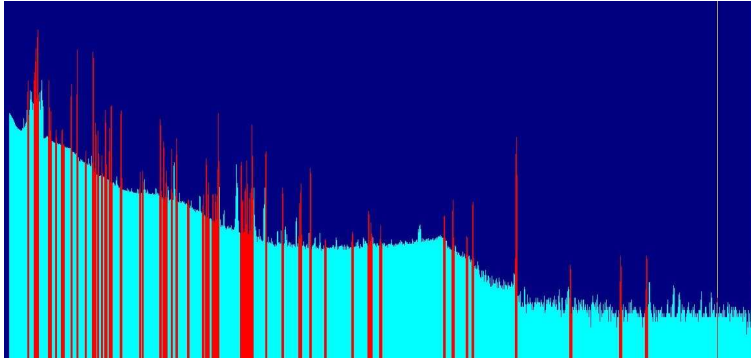


Figure 2.8: Gamma spectrum of one Uranium target after the irradiation

In table 2.7 the measurements results for the Uranium target compared with the MCB output results are reported.

Radionuclide	Measured activity (Bq)	MCB activity (Bq)
$^{238}\text{U}$	$4814 \pm 101$	$4799 \pm 480$
$^{235}\text{U}$	$244 \pm 5$	$224 \pm 22$
$^{239}\text{Np}$	$(3.36 \pm 0.7) \times 10^6$	$(3.95 \pm 0.39) \times 10^6$
$^{140}\text{Ba}$	$(2.13 \pm 0.45) \times 10^4$	$(1.9 \pm 0.19) \times 10^4$
$^{132}\text{Te}$	$(5.71 \pm 0.29) \times 10^4$	$(5.69 \pm 0.57) \times 10^4$
$^{131m}\text{Te}$	$(1.75 \pm 0.08) \times 10^4$	$(1.89 \pm 0.19) \times 10^4$
$^{131}\text{I}$	$(1.46 \pm 0.07) \times 10^4$	$(1.31 \pm 0.13) \times 10^4$
$^{99}\text{Mo}$	$(9.41 \pm 0.47) \times 10^4$	$(8.08 \pm 0.80) \times 10^4$
$^{99m}\text{Tc}$	$(1.87 \pm 0.09) \times 10^4$	$(22.22 \pm 0.22) \times 10^4$
$^{95}\text{Zr}$	$(4.87 \pm 0.25) \times 10^3$	$(3.15 \pm 0.31) \times 10^3$

Table 2.7: Comparison between measured and calculated activities using MCB code for natural Uranium target

In figure 2.9 the gamma spectrum of irradiated Thorium foil is shown.

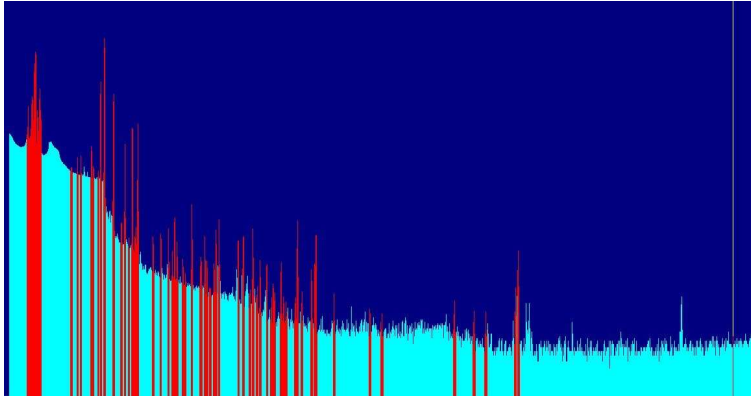


Figure 2.9: Gamma spectrum of one Thorium target after the irradiation

In table 2.8 are reported the measurements results for the Thorium target compared with the MCB output results.

Radionuclide	Measured activity (Bq)	MCB activity (Bq)
$^{232}\text{Th}$	$527 \pm 14$	$575 \pm 57$
$^{233}\text{Pa}$	$(1.78 \pm 0.04) \times 10^5$	$(1.69 \pm 0.17) \times 10^5$
$^{140}\text{Ba}$	$127 \pm 7$	$136 \pm 14$
$^{140}\text{La}$	$87 \pm 5$	$79 \pm 8$
$^{132}\text{Te}$	$284 \pm 94$	$126 \pm 13$
$^{131}\text{I}$	$44 \pm 6$	$23 \pm 2$

Table 2.8: Comparison between measured and calculated activities using MCB code for Thorium target

The uncertainties of the measured activities are evaluated by considering the statistical counting uncertainties and systematic uncertainties due to the target positioning on the detector and the detector efficiency. The uncertainties of MCB are evaluated by considering the flux uncertainties since the statistical uncertainties are negligible because we have considered  $10^7$  particles from the neutron source simulation.

## Irradiation at SM1 sub-critical complex

The SM1 subcritical complex (chapter 4) three groups integral flux for the irradiation channel A (ring 2) and channel B (ring 4) (2.10) are shown in tables 2.9 and 2.10.

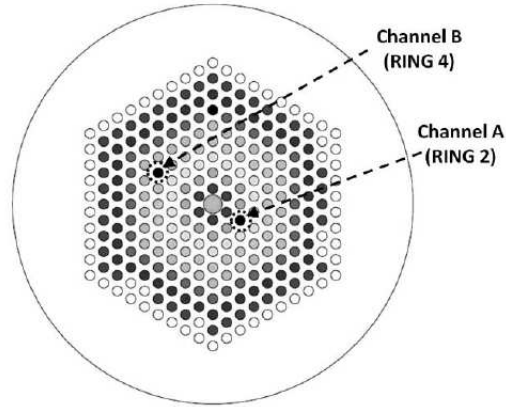


Figure 2.10: SM1 top view

Energy region	Energy intervals (MeV)	Integral flux ( $\text{n cm}^{-2}\text{s}^{-1}$ )
Thermal	$E \leq 0.55 \times 10^{-6}$	$(2.42 \pm 0.12) \times 10^4$
Epithermal	$0.55 \times 10^{-6} < E \leq 0.1$	$(1.65 \pm 0.08) \times 10^4$
Fast	$E > 0.1$	$(2.01 \pm 0.11) \times 10^4$

Table 2.9: SM1 subcritical complex integral flux composition (channel A)

Energy region	Energy intervals (MeV)	Integral flux ( $\text{n cm}^{-2}\text{s}^{-1}$ )
Thermal	$E \leq 0.55 \times 10^{-6}$	$(1.11 \pm 0.06) \times 10^4$
Epithermal	$0.55 \times 10^{-6} < E \leq 0.1$	$(7.5 \pm 0.38) \times 10^4$
Fast	$E > 0.1$	$(0.76 \pm 0.04) \times 10^4$

Table 2.10: SM1 subcritical complex integral flux composition (channel B)

The integral of SM1 flux fractions (%) in the three energy groups, with respect to the total, is shown in the next figure 2.11.

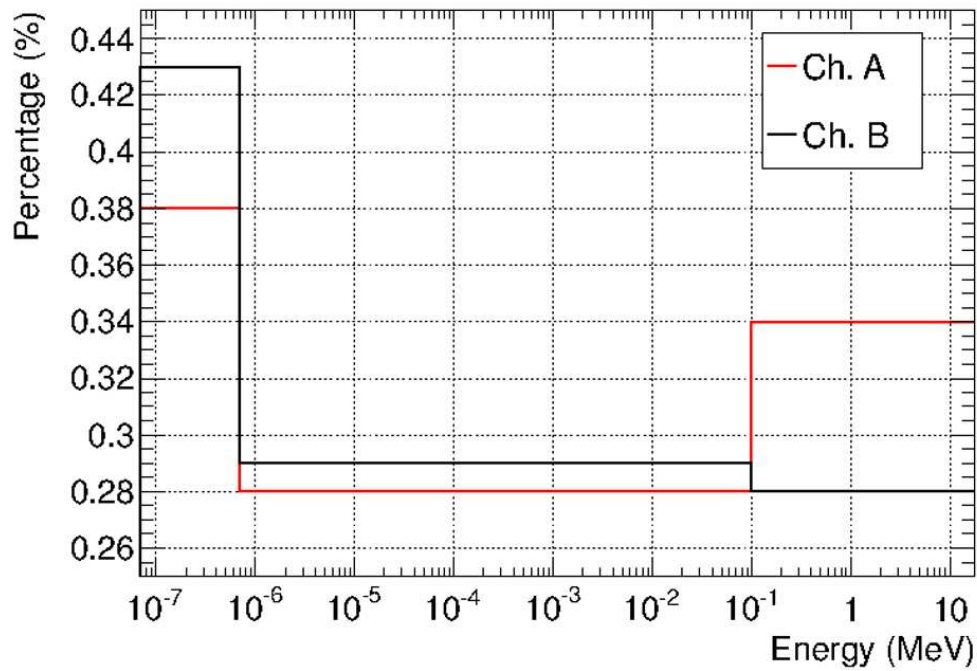


Figure 2.11: Three groups SM1 integral flux percentages in channels A and B

In figure 2.12 is instead shown the gamma spectrum of irradiated Uranium foil.

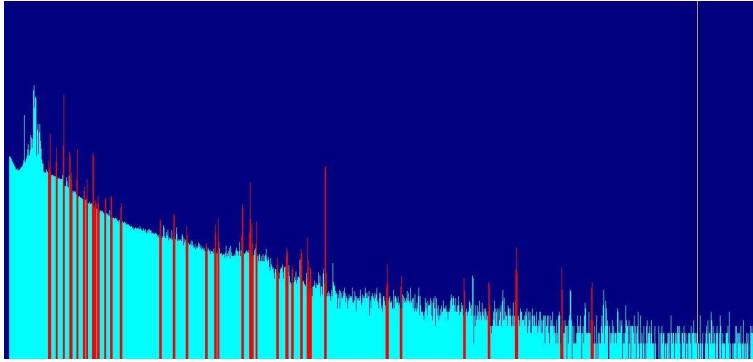


Figure 2.12: Gamma spectrum of one Uranium target after the irradiation

In table 2.11 are reported the measurements results for the Uranium target compared with the MCB output results.

Radionuclide	Measured activity (Bq)	MCB activity (Bq)
$^{238}\text{U}$	$4668 \pm 72$	$4835 \pm 145$
$^{235}\text{U}$	$216 \pm 6$	$225 \pm 7$
$^{239}\text{Np}$	$156 \pm 12$	$122 \pm 4$
$^{140}\text{Ba}$	$4.2 \pm 0.2$	$2.50 \pm 0.07$
$^{132}\text{Te}$	$3.78 \pm 0.48$	$3.5 \pm 0.11$
$^{131}\text{I}$	$2.6 \pm 0.3$	$2.10 \pm 0.06$
$^{99}\text{Mo}$	$5.4 \pm 0.8$	$4.32 \pm 0.13$
$^{99m}\text{Tc}$	$4.4 \pm 1.4$	$3.8 \pm 0.11$
$^{95}\text{Zr}$	$0.84 \pm 0.14$	$0.58 \pm 0.02$

Table 2.11: Comparison between measured and calculated activities using MCB code for natural Uranium target

In figure 2.13 the gamma spectrum of irradiated Uranium foil is shown.

### 2.3. MCB code: experimental validation

---

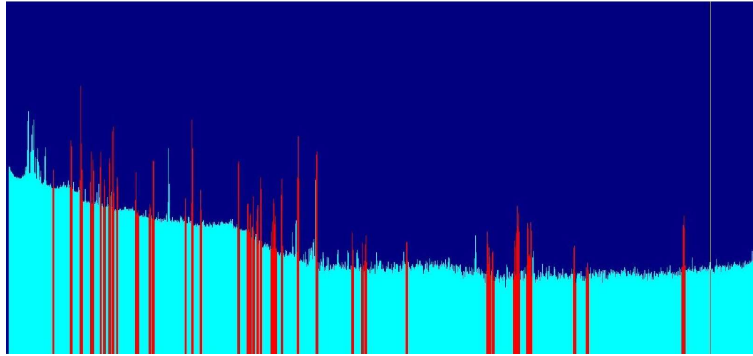


Figure 2.13: Gamma spectrum of one Thorium target after the irradiation

In table 2.12 the measurements results for the Thorium target compared with the MCB output results are reported.

Radionuclide	Measured activity (Bq)	MCB activity (Bq)
$^{232}\text{Th}$	$481\pm 11$	$528\pm 16$
$^{233}\text{Pa}$	$12.2\pm 0.4$	$12.43\pm 0.37$

Table 2.12: Comparison between measured and calculated activities using MCB code for Thorium target

The comparison between the analytically and measured activities for different nuclides gives a good results within the uncertainties and the systematic leakage for gaseous nuclides. MCB code is validated and ready to be used for burn-up calculations for TRIGA reactor and for SM1 sub-critical complex (chapters 3 and 4).



# Chapter 3

## Burn-up calculation for the TRIGA Mark II reactor

### 3.1 Experimental facility description

The TRIGA (Training Research and Isotope production General Atomics) Mark II is a pool-type research reactor moderated and cooled by light water. Fuel composition is made by a uniform mixture of Uranium (8%-wt), Hydrogen (1%-wt) and Zirconium (91%-wt); Uranium is enriched at 19,95%-wt in  $^{235}\text{U}$ . This composition gives the fuel a strong moderating property that property as well, that depends upon the fuel temperature: it decreases when the fuel temperature increases.

The TRIGA reactor of the University of Pavia has a nominal power of 250 kW in a steady-state operation. The core geometry of a right cylinder made of 90 locations distributed in 6 concentric rings. A radial section of TRIGA reactor core in the first charge configuration (i.e. 1965) is shown in figure 3.1. Rings are labelled as A (central hole), B, C, D, E and F, which respectively have 1, 6, 12, 18, 24 and 30 locations. These locations can be filled either with fuel elements (FE) or other core components like dummy elements (i.e. graphite elements), control rods, neutron source and irradiation channels (Central Thimble in the central hole and, in ring F, pneumatic transfer irradiation channel, named Rabbit, and Thimble F).

Reactor first core configuration consisted of 61 Al-clad fuel elements arranged in the core rings B (6 FE), C (11 FE), D (17 FE), E (23) and F (4 FE). Each fuel element has an external diameter of 3,75 cm and a total length of 72,24 cm, while the fuel diameter and height are respectively 3,61 cm and 35,6 cm (i.e. an active volume of about 364 cm<sup>3</sup>) as shown in figure 3.2. The dummy elements have size and shape as equal as fuel elements but are entirely filled with graphite. The active dimensions of the core are 45,7 cm in diameter and 35,6 cm in height for an active core volume of about  $5,84 \times 10^4$  cm<sup>3</sup>. A 30 cm thick radial graphite reflector surrounds the core while the axial reflector is provided by the fuel element itself in which two 10 cm graphite cylinders are located at the ends of the element. The radial graphite reflector includes a cavity that is used as an irradiation facility, named Lazy Susan. Light water, used as reactor coolant, contributes to neutron moderation inside the core volume and as axial and radial additional reflector (about 46 cm in the radial direction and 60 cm minimum in the axial downward direction). The reactor tank has a diameter of 1,98 m and an height of 6,4 m. The core reactivity is controlled by means of three absorbing rods, called SHIM (C ring), TRANSIENT (D ring) and REGULATING (E ring), made of boron carbide (SHIM, REG) and borated graphite (TRANS).

### 3.1. Experimental facility description

---

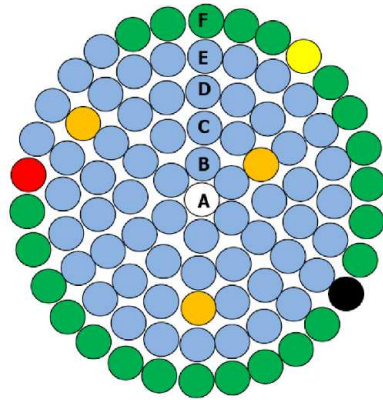


Figure 3.1: Radial section of TRIGA reactor core in the first charge configuration (1965): Fuel elements (light blue), dummy elements (green), Central Thimble (white), Rabbit (red), Thimble F (black), control rods (orange), neutron source (yellow)

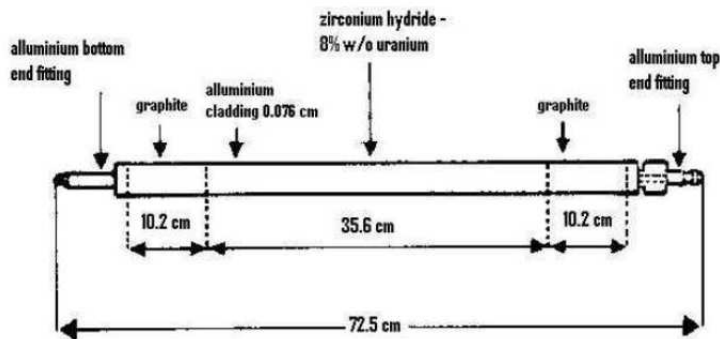


Figure 3.2: Fuel element characteristics

In figures 3.3 and 3.4 top and side views of the reactor are sketched, including the radial channels, the thermal and thermalizing columns. These elements are useful in order to irradiate some big samples or to have a different neutron flux distribution with respect to in-core channels fluxes distribution.

### 3. Burn-up calculation for the TRIGA Mark II reactor

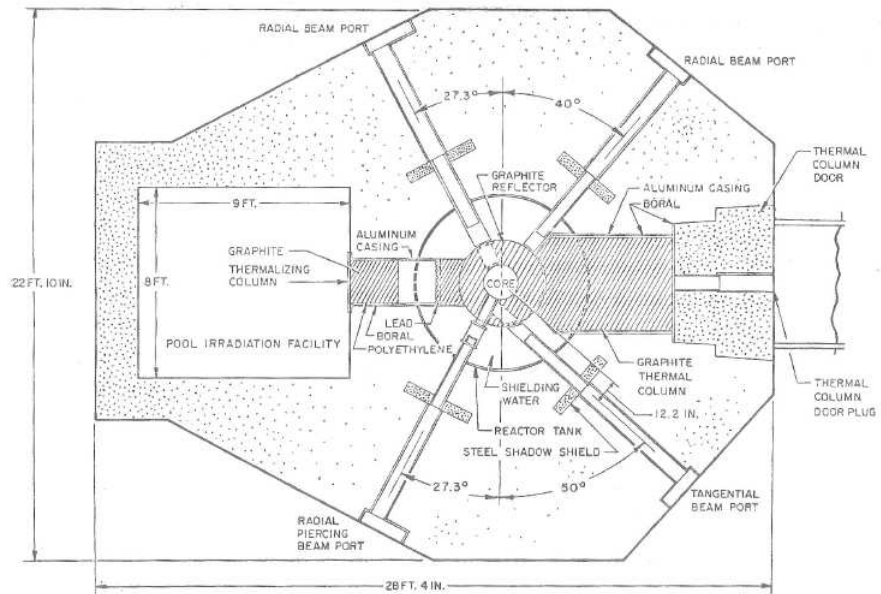


Figure 3.3: TRIGA reactor top view

### 3.2. Neutron fluxes evaluation

---

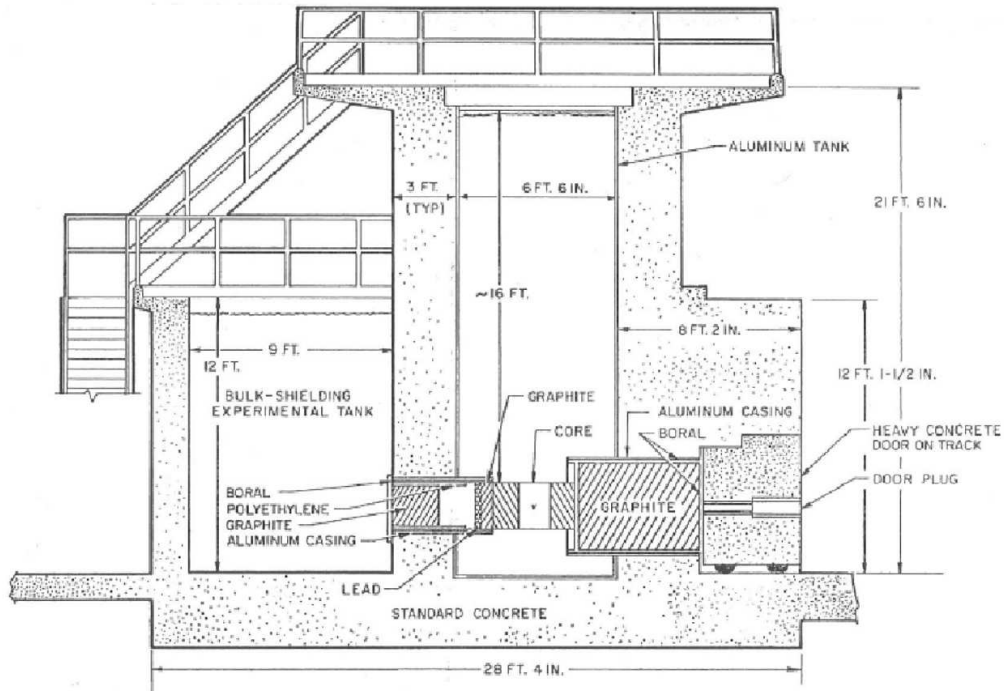


Figure 3.4: TRIGA reactor side view

## 3.2 Neutron fluxes evaluation

TRIGA in-core neutron fluxes evaluation (Central, Rabbit and Lazy Susan channels) is performed through the irradiation of samples in each of three irradiation positions [10]. The method here used is the standard stacked-foil activation technique. It is based on a set of different type of materials, in order to measure the neutron flux covering the whole neutron energy spectra. The different nuclear reactions induced in the materials used for this work are reported in table 3.1.

### 3. Burn-up calculation for the TRIGA Mark II reactor

Element	Isotope	Isotopic abundance	Reaction	$E_{act}(MeV)$	$T_{\frac{1}{2}}$
Au	$^{197}\text{Au}$	100%	$^{197}\text{Au}(n,\gamma)^{198}\text{Au}$	0	2.7 d
Cu	$^{63}\text{Cu}$	69.1%	$^{63}\text{Cu}(n,\gamma)^{64}\text{Cu}$	0	12.7 h
Fe	$^{54}\text{Fe}$	5.84%	$^{54}\text{Fe}(n,p)^{54}\text{Mn}$	3.75	312.1 d
Ni	$^{58}\text{Ni}$	68.08%	$^{58}\text{Ni}(n,p)^{58}\text{Co}$	2.5	
In	$^{115}\text{In}$	95.71%	$^{115}\text{In}(n,n')^{115m}\text{In}^*$	1.65	4.5 h
Al	$^{27}\text{Al}$	100	$^{27}\text{Al}(n,p)^{27}\text{Mg}$	5.30	9.5 min

Table 3.1: Neutron activation reaction characteristics

In figure 3.5 [4] is shown the  $^{197}\text{Au}(n,\gamma)^{198}\text{Au}$  and  $^{63}\text{Cu}(n,\gamma)^{64}\text{Cu}$  reactions cross sections.

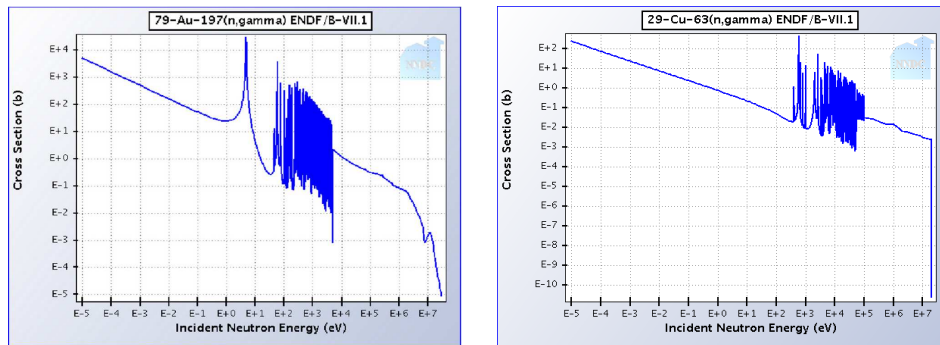


Figure 3.5:  $^{197}\text{Au}(n,\gamma)^{198}\text{Au}$  (left) and  $^{63}\text{Cu}(n,\gamma)^{64}\text{Cu}$  (right) reactions cross sections as a function of incident neutron energy [4]

In figure 3.6 [4] the  $^{54}\text{Fe}(n,p)^{54}\text{Mn}$  and  $^{58}\text{Ni}(n,p)^{58}\text{Co}$  reactions cross section are shown.

### 3.2. Neutron fluxes evaluation

---

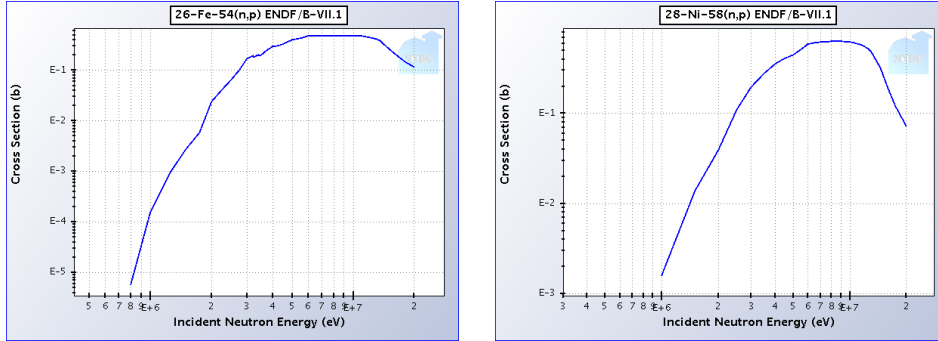


Figure 3.6:  $^{54}\text{Fe}(n,p)^{54}\text{Mn}$  (left) and  $^{58}\text{Ni}(n,p)^{58}\text{Co}$  (right) reactions cross sections as a function of incident neutron energy [4]

In figure 3.7 [4] is shown the  $^{115m}\text{In}(n,n')^{115m}\text{In}$  and  $^{27}\text{Al}(n,p)^{27}\text{Mg}$  cross sections.

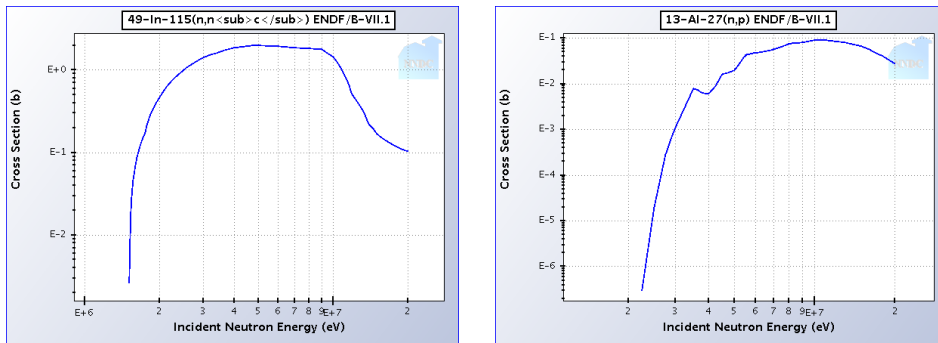


Figure 3.7:  $^{115m}\text{In}(n,n')^{115m}\text{In}$  (left) and  $^{27}\text{Al}(n,p)^{27}\text{Mg}$  (right) reactions cross sections as a function of incident neutron energy [4]

After the irradiation, the activated nuclides are in an excited state and are able to decay by emission of gamma radiation [12,13,14].

In order to process the experimental data with the SAND II code, it was necessary to evaluate the specific activity at saturation. [11]. This code, starting from specific saturation activity and from a guess flux, is able to evaluate a differential neutron flux in 621 points. The differential flux obtained using SAND II code is independent of the integral values of the guess flux but

there is a strong dependence of the epithermal flux region by the flux form while thermal and fast flux regions are invariant [10].

### 3.2.1 Specific saturation activity

Once known the irradiation time  $T_{irr}$  in the specific TRIGA irradiation channel, the time interval between the end of irradiation and the beginning of the counting  $\Delta T$ , and the counting time  $T_{count}$ , the induced activity  $A_{EOI}$  at the end of irradiation (EOI), it was possible to the specific activity at saturation  $A_{spec-sat}$ , for each foil [15,16,17]. The value of the measured activity  $A_{meas}$ , obtained with gamma spectrometry, has been corrected by a factor that takes into account the decay during the counting. The factor that gives this correction is given by:

$$F_{count} = \frac{\lambda T_{count}}{1 - e^{-\lambda T_{count}}} \quad (3.1)$$

where  $\lambda$  is the decay constant of the specific nuclide. Thus, the product  $F_{count}A_{meas}$  gives the initial activity  $A_{in}$ . The second step is to evaluate the activity at EOI, allowing to compare the various measurement taken for each single target foil. The activity at EOI is obtained multiplying the quantity  $A_{in}$  by the correction factor given by

$$F_{\Delta T} = \frac{1}{e^{-\lambda \Delta T}} \quad (3.2)$$

which leads to  $A_{EOI} = F_{\Delta T} A_{in} = F_{\Delta T} F_{count} A_{meas}$ .

Once  $A_{EOI}$  is obtained, it was straightforward to evaluate the specific activity  $A_{spec}$  with the formula:

$$A_{spec} = \frac{A_{EOI} m_A}{m N_A} \quad (3.3)$$

where  $m_A$  is the atomic mass of the element under consideration for neutron activation,  $m$  is the target foil mass and  $N_A$  is the Avogadro's number. Finally, multiplying by the saturation factor,  $F_{irr}$ , it is possible to define the specific activity at saturation:

$$A_{spec-sat} = A_{spec} F_{irr} = \frac{A_{spec}}{1 - e^{-\lambda T_{irr}}} \quad (3.4)$$

where  $T_{irr}$  is the irradiation time in seconds.

### 3.2.2 Attenuation coefficient

For elements with a high neutron capture cross section, as gold, the intensity of the flux inside of the target foil decreases with increasing thickness, due to the high number of neutron capture processes inside the material. In these cases the calculated activity that results is less than that which would occur if the flux through the target foils was constant for the entire thickness. In order to avoid an underestimation of the incident flux, it is therefore necessary to correct the calculations for this effect.

To evaluate the attenuation coefficient a dedicated set of simulations, by means of the Monte Carlo code MCNP, were performed using the feature of the Inward Cosine card. This option allows to create a neutron source distributed over a closed surface (in our case a sphere) so that the neutron fluence inside the volume bounded by the surface is constant. In the case of a sphere, the neutron fluence inside the volume is equal to  $1/R^2$ , where R is the radius of the sphere. A cell, with the same geometry of the gold target foil, in the center of the sphere was located. Using this geometry, several simulations were performed filling the target cell with gold material with different densities, starting with the density of metallic gold and reducing it each time by a factor of 10.

For all simulations the neutron capture density, defined as the number of neutron captures into the target cell divided by the number of atoms of gold contained into the cell, was calculated. These simulations show that the neutron capture density reaches a constant value starting from a material density dilution of a factor of  $10^4$ . When this condition is achieved it means that the self-absorption effect in the material is negligible. Thus dividing the neutron capture density calculated with the metallic gold target by the constant value obtained after material dilution, the attenuation coefficient  $C_{att}$  was evaluated. The results provided by the simulations for the attenuation coefficient was  $C_{att} = 0.88$ . The value of specific activity at saturation for gold has been then further divided by the factor  $C_{att}$  to obtain the correct value of activity to be included in the input file for SAND II. The attenuation coefficients for the other foils are considered to be  $C=1$  because there is not self-absorption.

#### 3.2.3 Flux uncertainties evaluation

Neutron flux uncertainties have been estimated by considering systematic and statistic contributions.

Systematic uncertainties is evaluated by considering the following contributions:

- Due to the optimization of irradiation and counting time of the foils, statistical uncertainties of the measurements together with uncertainties related to the detector efficiency calibration are evaluated to be less than 3%. The systematic error due to the positioning of the foils on the detector was investigated separately performing several repeated measurements of an irradiated foil of copper, every time repositioning it on the detector. The evaluated error are less than 2% giving a total uncertainty of the gamma spectrometry measurements about 5%.
- Measurements of the weights of the foils are performed using an analytical balance with an accuracy in the order of 0.05 mg. Thus, the evaluated uncertainties related to the determination of the weight of the foils are about 1% for gold foils and much less than 1% for the foils of other materials.
- Thermal power calibration of the reactor is performed according to the specific procedure using certified instrumentation. Taking into account all the uncertainties of the procedure, the power calibration measurement is affected by an uncertainty of about 3%. The reactor power automatic control allows to maintain the power level during the irradiation of the samples with a precision of 0.5%.

The evaluated total systematic uncertainties are about 8.5%.

The SAND II program gives as result a differential neutron spectrum without uncertainties. The method adopted in this work to calculate the propagation of statistic uncertainties of the foils measurements in the de-convolution process, is based on a multiple run (100 for each irradiation position) of the SAND II program with different sets of measured activities input data. The set of values are calculated fitting a Student's t-distribution with mean equal to the average measured activity and standard deviation equal to the uncertainty

## 3.2. Neutron fluxes evaluation

---

of the gamma spectrometry measurement: one hundred differential neutron flux densities for each irradiation position are calculated and, for each energy average value and the variance are evaluated. The average flux differential density evaluated in this way is affected by a standard deviation less than 2%. The group flux densities are evaluated integrating the average flux differential densities and the uncertainties over the energy group are evaluated according to the error propagation rules.

This evaluation is used in the uncertainties evaluation for each TRIGA and SM1 irradiation channel.

### 3.2.4 Central channel flux evaluation

In order to evaluate neutron flux in TRIGA central thimble, the Copper, Copper (Cd) (covered with Cadmium in order to cut the flux thermal component), Gold, Gold (Cd) and Nickel foils have been irradiated using a reactor power of 2.5 kW, while Iron, Indium and Aluminum foils have been irradiated with 25 kW reactor power. Copper and Gold foils have been irradiated also covered by Cadmium in order to reduce the thermal flux component.

In table 3.2 the mean specific saturation activities values at 250 kW nominal reactor power in central channel are reported.

Element	$A_{spec-sat}$ (Bq) P=250 kW
Cu	$(2.56 \pm 0.13) \times 10^{-11}$
Cu (Cd)	$(7.58 \pm 0.38) \times 10^{-12}$
Au	$(1.14 \pm 0.06) \times 10^{-9}$
Au (Cd)	$(4.97 \pm 0.25) \times 10^{-10}$
Ni	$(3.45 \pm 0.17) \times 10^{-13}$
Fe	$(3.21 \pm 0.16) \times 10^{-13}$
In	$(8.30 \pm 0.42) \times 10^{-13}$
Al	$(1.67 \pm 0.09) \times 10^{-14}$

Table 3.2: Specific saturation activities values for each irradiated foil in central channel, the values of specific saturation activity affected by uncertainty of 5%

These values are inserted in SAND II code, in order to have a flux evaluation, the results are shown in figure 3.8.

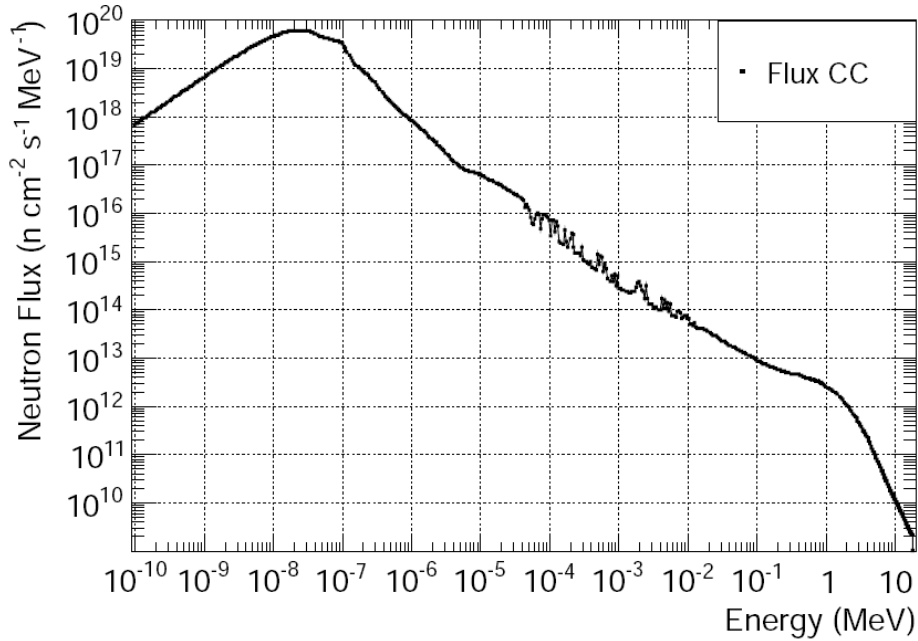


Figure 3.8: Differential flux in central thimble of TRIGA reactor

The integral flux is  $(2.156 \pm 0.004 \text{ (stat)} \pm 0.18 \text{ (syst)}) \times 10^{13} \text{ n cm}^{-2} \text{ s}^{-1}$ .

### 3.2.5 Rabbit channel flux evaluation

In table 3.3 are reported the mean specific saturation activities values at nominal TRIGA reactor power 250 kW in the Rabbit irradiation channel.

### 3.2. Neutron fluxes evaluation

Element	$A_{spec-sat}$ (Bq) P=250 kW
Cu	$(1.23 \pm 0.06) \times 10^{-11}$
Cu (Cd)	$(3.63 \pm 0.18) \times 10^{-12}$
Au	$(5.15 \pm 0.26) \times 10^{-10}$
Au (Cd)	$(2.29 \pm 0.12) \times 10^{-10}$
Ni	$(1.44 \pm 0.07) \times 10^{-13}$
Fe	$(1.20 \pm 0.06) \times 10^{-13}$
In	$(3.20 \pm 0,16) \times 10^{-13}$
Al	$(5.63 \pm 0,28) \times 10^{-15}$

Table 3.3: Specific saturation activities values for each irradiated foil in Rabbit channel, the values of specific saturation activity affected by uncertainty of 5%

These values are inserted in SAND II code, in order to have a flux evaluation: the results are shown in figure 3.9.

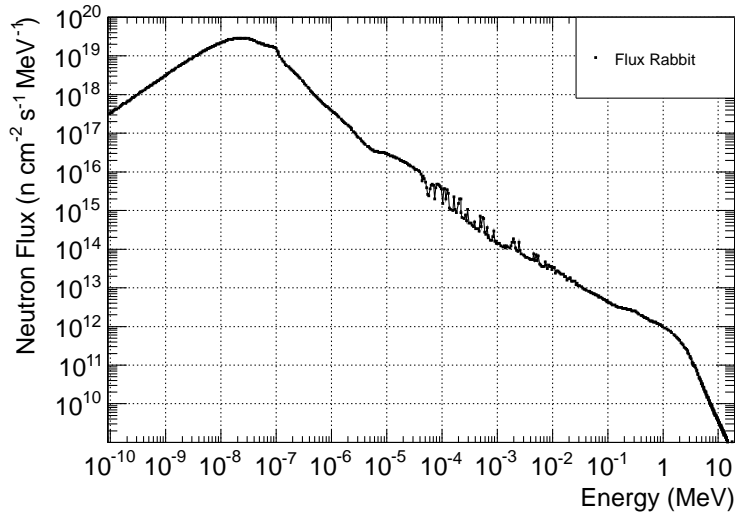


Figure 3.9: Differential flux in Rabbit irradiation channel of TRIGA reactor

The integral flux is  $(9.77 \pm 0.03 \text{ (stat)} \pm 0.83 \text{ (syst)}) \times 10^{12} \text{ n cm}^{-2} \text{ s}^{-1}$ .

### 3.2.6 Lazy Susan channel flux evaluation

In table 3.4 are reported the mean specific saturation activities values at nominal TRIGA reactor power 250 kW in the Lazy Susan irradiation channel.

Element	$A_{spec-sat}$ (Bq) P=250 kW
Cu	$(4.30 \pm 0.21) \times 10^{-12}$
Cu (Cd)	$(1.71 \pm 0,08) \times 10^{-12}$
Au	$(1.83 \pm 0,09) \times 10^{-10}$
Au (Cd)	$(7.53 \pm 0.38) \times 10^{-11}$
Ni	$(2.01 \pm 0,11) \times 10^{-14}$
Fe	$(1.76 \pm 0.09) \times 10^{-14}$
In	$(5.59 \pm 0.28) \times 10^{-14}$
Al	$(8.36 \pm 0.42) \times 10^{-16}$

Table 3.4: Specific saturation activities values for each irradiated foil in Lazy Susan channel, the values of specific saturation activity affected by uncertainty of 5%

These values are inserted in SAND II code, in order to have a flux evaluation, the results are shown in figure 3.10.

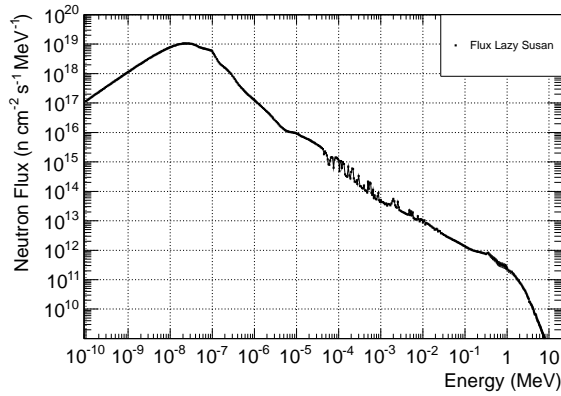


Figure 3.10: Differential flux in Lazy Susan irradiation channel of TRIGA reactor

### 3.3. Fuel burn-up analytical evaluation

---

The integral flux is  $(3.11 \pm 0.01 \text{ (stat)} \pm 0.26 \text{ (syst)}) \times 10^{12} \text{ n cm}^{-2} \text{ s}^{-1}$ .

In figure 3.11 the differential flux distribution in the three irradiation channels of TRIGA reactor is shown.

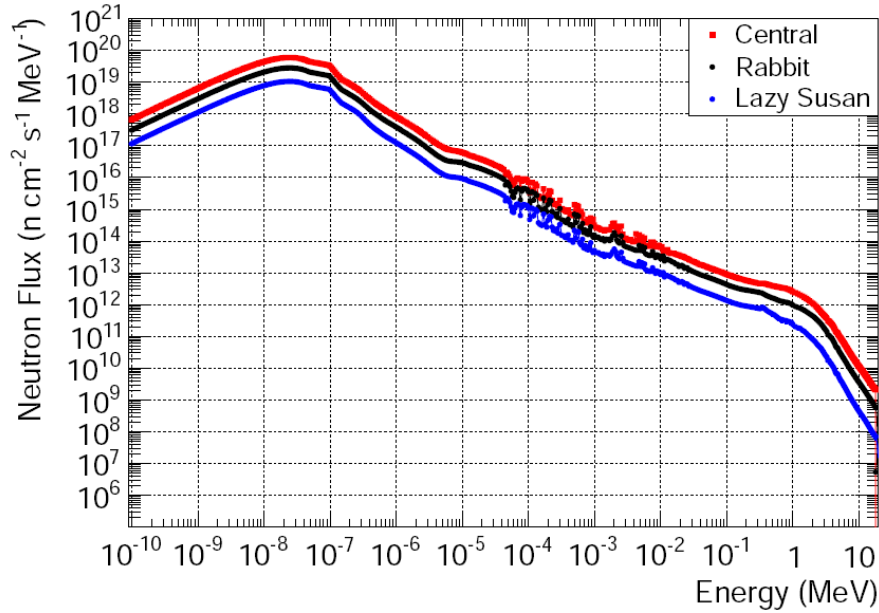


Figure 3.11: Differential flux in the three irradiation channels of TRIGA reactor

### 3.3 Fuel burn-up analytical evaluation

In this section the TRIGA Mark II reactor burn-up analytical evaluation will be described [18,19]. In order to evaluate the fuel burn-up it is necessary to know the neutron flux inside fuel elements. Neutron flux is evaluated by means of MCNP code [20] in each fuel element and, as an average, in each core ring (B, C, D, E and F). In figure 3.12 the neutron flux densities in each ring, grouped into 40 energy intervals and evaluated at 250 kW reactor power are

### 3. Burn-up calculation for the TRIGA Mark II reactor

shown. Results are affected by a statistical uncertainty on each energy group less than 1% and by a statistical uncertainty on the entire value less than 0,2%.

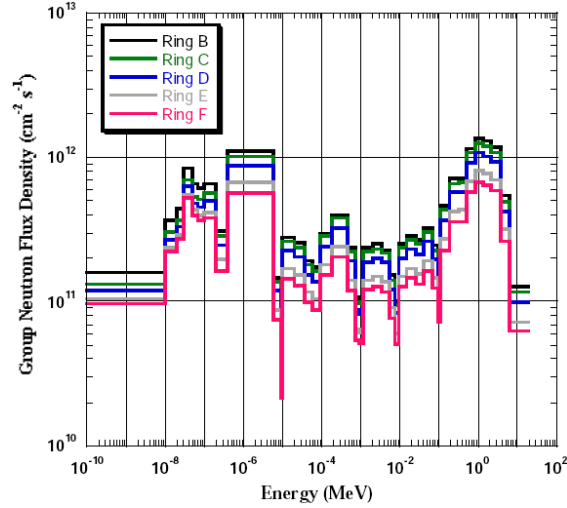


Figure 3.12: Neutron flux density in each core ring at 250 kW reactor power

Effective microscopic cross sections  $\sigma_{eff}$  were calculated for each  $i$ -th core ring (from B to F) as

$$\sigma_i^{eff} = \frac{\sum_{j=1}^{40} \sigma_j \Phi_{i,j}}{\sum_{j=1}^{40} \Phi_{i,j}} \quad (3.5)$$

where  $\sigma_j$  is the value of the microscopic cross sections averaged over the  $j$ -th energy group and  $\Phi_{i,j}$  is the group neutron flux in each core ring (shown in figure 3.12). The average microscopic cross sections were computed using data available in literature [21], while the group neutron flux density in each core ring was evaluated by means of MCNP. The values of the effective microscopic cross sections for fission reaction, radiative capture and absorption are reported in tables 3.5 and 3.6. Values are affected by an uncertainty evaluated as propagation of statistical uncertainties on group neutron flux densities.

### 3.3. Fuel burn-up analytical evaluation

---

As recalled before, the total neutron flux in each core ring was evaluated by MCNP while the reaction rates (R) were calculated as the product  $\sigma^{eff} \cdot \Phi_{tot}$  (values are also shown in table 3.6). The uncertainties on reaction rates values are evaluated as propagation of statistical uncertainties on the effective microscopic cross sections.

The  $^{235}\text{U}$  effective microscopic cross sections averaged over the whole core were calculated weighting the data of tables 3.5 and 3.6 over the fractional number of fuel elements in each core ring. Calculated values show, within the uncertainties, a good agreement with data taken from literature (table 3.7)

Ring	$\sigma_{(n,f)}^{eff}$ (b)	$\sigma_{(n,\gamma)}^{eff}$ (b)	$\sigma_{abs}^{eff}$ (b)
B	102.6±2.6	20.8±0.5	123.4±4.5
C	95.0±2.0	19.5±0.4	114.5±3.4
D	97.6±1.8	20.0±0.4	117.6±3.1
E	109.6±2.1	22.1±0.4	131.7±3.5
F	117.2± 4.4	23.4±0.9	140.6±7.6

Table 3.5:  $^{235}\text{U}$  effective microscopic cross section ( $\sigma^{eff}$ ) in each reactor core ring

Ring	$\Phi_{tot}$ ( $\text{cm}^{-2}\text{s}^{-1}$ )	$R_{abs}$ ( $\text{s}^{-1}$ )	$R_{fiss}$ ( $\text{s}^{-1}$ )
B	$1.74 \times 10^{13}$	$(2.15 \pm 0.08) \times 10^{-9}$	$(1.79 \pm 0.05) \times 10^{-9}$
C	$1.58 \times 10^{13}$	$(1.81 \pm 0.05) \times 10^{-9}$	$(1.50 \pm 0.03) \times 10^{-9}$
D	$1.37 \times 10^{13}$	$(1.61 \pm 0.04) \times 10^{-9}$	$(1.34 \pm 0.03) \times 10^{-9}$
E	$1.06 \times 10^{13}$	$(1.40 \pm 0.04) \times 10^{-9}$	$(1.16 \pm 0.02) \times 10^{-9}$
F	$0.91 \times 10^{13}$	$(1.28 \pm 0.07) \times 10^{-9}$	$(1.07 \pm 0.04) \times 10^{-9}$

Table 3.6: Total neutron flux ( $\Phi_{tot}$ ) and reaction rates (R) in each reactor core ring (neutron flux statistical uncertainties are 0.2%)

### 3. Burn-up calculation for the TRIGA Mark II reactor

	$\sigma_{(n,f)}^{eff}$ (b)	$\sigma_{(n,\gamma)}^{eff}$ (b)	$\sigma_{n,\gamma}^{eff}/\sigma_{n,f}^{eff}$ (b)
MCNP	103.43±5.89	21.00±1.20	0.203±0.016
Al-clad	100.20	19.50	0.195
SST-clad	107.90	20.87	0.193

Table 3.7: Calculated average microscopic cross sections (MCNP) compared to Al-clad and SST-clad FE values reported in literature

For each TRIGA fuel element the Uranium content and enrichment is known from manufacturer while the number of hours of operation in a specific core position are reported in the reactor log-book.

For each fuel element the  $^{235}\text{U}$  nuclei consumption ( $N_{con}$ ) has been calculated according to the formula

$$N_{con} = \frac{mN_A}{235} [(1 - e^{-R_{abs,BtB}}) + (1 - e^{-R_{abs,CtC}}) + (1 - e^{-R_{abs,DtD}}) + (1 - e^{-R_{abs,EtE}}) + (1 - e^{-R_{abs,FtF}})] \quad (3.6)$$

where  $m$  is the Uranium content of each fuel element (in grams),  $N_A$  is the Avogadro's number,  $R_{abs}$  is the total absorption rate in each core ring shown in table 3.6 and  $t$  is the time of operation of the fuel element in each core ring (from B to F) in seconds. In a similar way, the nuclei of  $^{235}\text{U}$  fissioned ( $N_{Bu}$ ) have been calculated for each fuel element as

$$N_{Bu} = \frac{mN_A}{235} [(1 - e^{-R_{abs,BtB}}) \frac{\sigma_{f,B}}{\sigma_{abs,B}} + (1 - e^{-R_{abs,CtC}}) \frac{\sigma_{f,C}}{\sigma_{abs,C}} + (1 - e^{-R_{abs,DtD}}) \frac{\sigma_{f,D}}{\sigma_{abs,D}} + (1 - e^{-R_{abs,EtE}}) \frac{\sigma_{f,E}}{\sigma_{abs,E}} + (1 - e^{-R_{abs,FtF}}) \frac{\sigma_{f,F}}{\sigma_{abs,F}}] \quad (3.7)$$

### 3.4. Fuel burn-up calculation using MC codes

---

where the effective microscopic cross sections evaluated in each core ring (form B to F) are those shown in table 3.5.

The calculations were performed for all fuel elements introduced in the reactor core since the first criticality (November 15th 1965) up to December 31st 2008, for a total of 97 fuel elements. Results of the calculations gave a total of  $370.8 \pm 11.5$  g of fissioned  $^{235}\text{U}$  and a total of  $446.1 \pm 13.9$  g of consumed  $^{235}\text{U}$  over 32044 hours of reactor operation at full power (i.e. 250 kW). Uncertainties were evaluated as the results of propagation of Monte Carlo statistical uncertainties results into the analytical calculations.

A rough comparison of this result can be done simply evaluating the mass of fissioned  $^{235}\text{U}$  using the approximate relation based on total energy release, i.e. 1,05 g/MWd. Since the reactor was in operation for 32044 hours at 250 kW, the total energy released during this period was equal to 333,79 MWd. By using the approximate relation, this amount of released energy gives a total mass of  $^{235}\text{U}$  fissioned equal to 350.5 g. This estimation, within the uncertainties, shows a fairly good agreement with the calculations based on Monte Carlo code (i.e.  $370.8 \pm 11.6$  g of fissioned  $^{235}\text{U}$ ).

## 3.4 Fuel burn-up calculation using MC codes

In this section the simulation methodology used in order to have a burn-up estimation in TRIGA reactor will be described.

In order to have a burn-up evaluation of each TRIGA fuel element, it is fundamental to know the neutron flux values in each fuel element (FE) during its life inside the reactor core. That is done using MCNP code, which is able to give such kind of informations. From 1965 to 2012 the reactor core has assumed 30 different configurations therefore it is not possible to have the correct composition of each FE after each reconfiguration: the methodology used in this work consists in the research of a correct neutron flux distribution

which takes in account the different positions and times by which the FE has been irradiated [29].

The simulation of irradiation of each FE has been performed using MCB code with an input flux distribution obtained by considering the neutron flux in each position weighted average on the irradiation time in this position.

#### 3.4.1 Simulations description

The MCB irradiation simulations are performed with the following characteristic:

- Geometry: a sphere (R=1.5 cm) surrounded by another sphere (R=20 cm): the neutron source (with the average spectrum described before) is uniformly distributed on the surface of the external sphere.
- The fuel consist in a Uranium-Zirconium hydride alloy with density diluted by 100 factor in order to reduce auto-absorption phenomena.
- The irradiation time is the time of permanence of each FE inside the reactor core.
- The number of neutron emitted from the source in each simulation is  $10^8$  in order to ensure a good MC statistic.

The results from MCB are the masses of all nuclides produced in the FE; only the most relevant are considered in order to determine the fuel composition.

- Structural materials:  $^{235}\text{U}$ ,  $^{238}\text{U}$  and ZrH.
- Transuranic nuclides:  $^{239}\text{Pu}$  (fissile)
- Saturable poisons:  $^{149}\text{Sm}$  and  $^{151}\text{Sm}$  ( $\sigma_a=4\times 10^5$  b and  $1.5\times 10^5$  b respectively). In this contest  $^{135}\text{Xe}$  and  $^{157}\text{Gd}$  are not considered because the first has a mean life time of 9 hours and the second is produced in a negligible quantity. In this work the  $^{151}\text{Sm}$  has not been considered, because the ratio between decay and the decrease contribution is about 1.4%.

### 3.4. Fuel burn-up calculation using MC codes

---

- Non-saturable poisons: as reported in literature, all non-saturable fission products can be grouped in a lump fission product [22] with  $\sigma_a=50$  b in each fission. This stable nuclide, e.g. the  $^{45}\text{Sc}$ . We have estimated that the concentration of lump fission product is 2.7  $^{45}\text{Sc}$  nuclei for each fission.

From the irradiation of 97 FE we obtained the following results: (444.7±44.5) g of  $^{235}\text{U}$  have been consumed while (372.3±37.2) g have been fissioned, producing an energy of 354.5 MWd. The FE mean burn-up (ratio between the  $^{235}\text{U}$  present mass and  $^{235}\text{U}$  initial mass) is about 10%. Furthermore from calculations, (94.6±9.5) g of  $^{238}\text{U}$  are consumed, assuming that all the consumed  $^{238}\text{U}$  has formed  $^{239}\text{Pu}$ , a total of 6.2 g of  $^{239}\text{Pu}$  have contributed to fission process.

In order to validate experimentally this calculation methodology, three different configurations have been simulated using MCB code, and the results have been compared with *core excess* measurements in this three different configurations.

Core excess represents the reactivity still available when the reactor is critical at zero power <sup>1</sup>. For example in the case of TRIGA this measurement is performed at P=1.5 W (without temperature effects) with the partial insertion of REG and SHIM control rods while TRANSIENT (see figure 3.1) rod is completely extracted. Total rods reactivity (6.13 \$, see paragraph 1.6.2) minus the core excess value is the so called shutdown margin that represent the total amount of reactivity that has to be inserted in the core in order to reach the critical condition at zero power.

For a practical description of core excess see figure 3.13

---

<sup>1</sup>Zero power means a reactor power where temperature effects and poisoning effects are not present. For a TRIGA reactor this power is commonly in the range 1-100 Watt

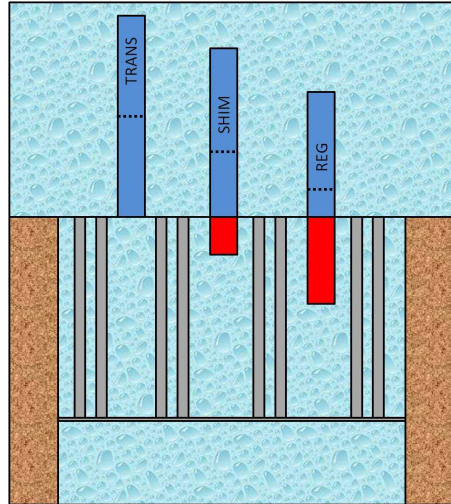


Figure 3.13: Scheme for a practical representation of the core excess concept: the red portions of the control rods represent the core excess that is the sum of the residual reactivities of the control rods when the reactor is critical at zero power; blue portions represents the shut-down margin that is the reactivity available to shut-down the reactor, gray bars represent the fuel elements

The total amount of reactivity controlled by each rod is shown in table 3.8.

Rod	$\rho$ (\$)
SHIM	3.09
TRANS	1.95
REG	1.09
Total	6.13

Table 3.8: Reactivity value of each TRIGA reactor control rod

In particular from the core excess comparison between simulations and measurements it is evident, from the first charge configuration (1965), a 0.42 \$ discrepancy. This can be associated with geometric approximations and materials impurities which are not considered in the MCB/MCNP simulations. The offset of 0.42 \$ has been applied to all measurements to have into consideration

### 3.4. Fuel burn-up calculation using MC codes

non impurities of real materials. If we subtract this offset value for the other 2 configurations (2009 and 2012), it is easy to see that the values are compatible within measurement errors. This results are shown in table 3.9.

Configuration	$\rho_{sim}$ (\$)	$\rho_{sim}$ -offset (\$)	$\rho_{meas}$ (\$)
16/11/1965	$3.44 \pm 0.04$	$3.02 \pm 0.04$	$3.02 \pm 0.06$
20/01/2009	$2.90 \pm 0.04$	$2.48 \pm 0.04$	$2.45 \pm 0.05$
20/01/2012	$2.67 \pm 0.04$	$2.25 \pm 0.04$	$2.26 \pm 0.04$

Table 3.9: Measurements and simulations core excess reactivity results

In figure 4.1 percentage burn-up of all TRIGA elements in a top core view is shown.

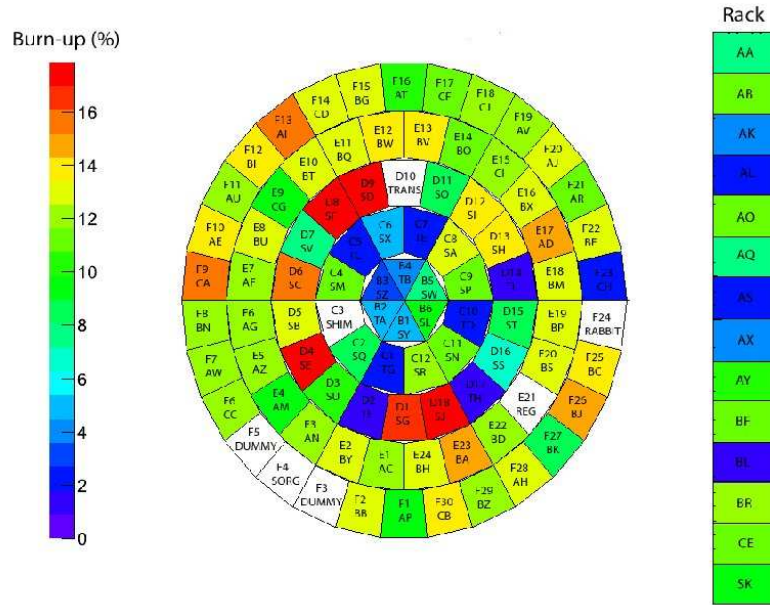


Figure 3.14: Schematic view of percentage burn-up for all TRIGA FE, letters are identificative codes for fuel element and positions in the grid

### 3. Burn-up calculation for the TRIGA Mark II reactor

A greater core excess makes it possible an extension of reactor life because the core excess decrease increasing burn-up.

In order to have a greater core excess in TRIGA reactor some simulations with different configurations have been performed, respecting the following safety rules:

- $CE (\$) < (SHIM (\$) + TRANS (\$) + REG (\$)) / 2$
- $TRANS (\$) + REG (\$) - CE (\$) > 0.50 \$$

where CE (\$) is the core excess, SHIM (\$), TRANS (\$) and REG (\$) are the values in dollars for reactivity associated with the three reactor control rods.

The best core configuration is shown in figure 4.2

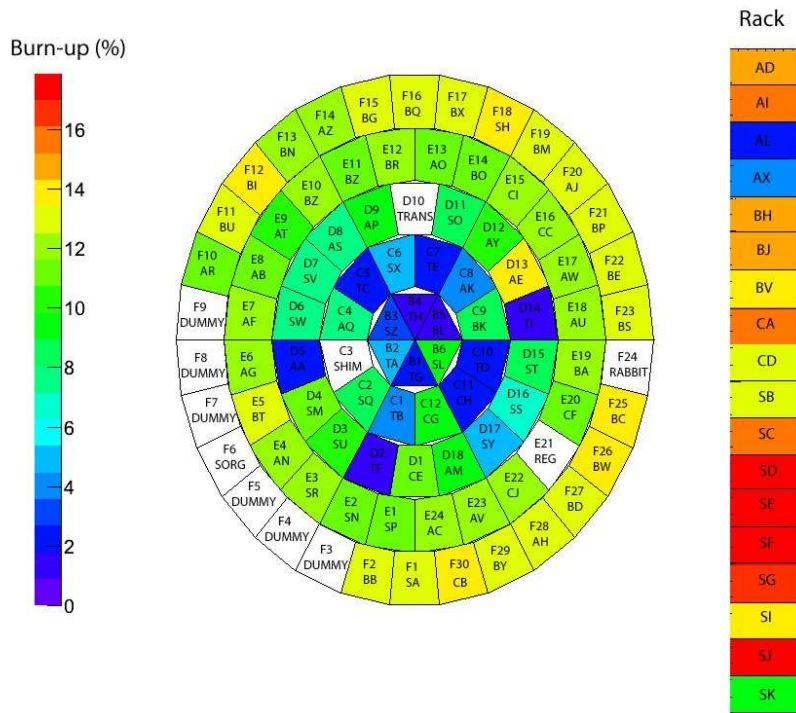


Figure 3.15: Schematic view of percentage burn-up for all TRIGA FE in the new configuration

### 3.4. Fuel burn-up calculation using MC codes

---

In this new configuration the core excess value is 3.03 \$ while the reactivity of each rod is shown in table 3.10.

Rod	$\rho$ (\$)
SHIM	3.09
TRANS	2.39
REG	1.23
Total	6.71

Table 3.10: Reactivity value of each TRIGA reactor control rod in the new configuration

### 3. Burn-up calculation for the TRIGA Mark II reactor

---

# Chapter 4

## Characterization of the SM1 subcritical Multiplying complex

The thermal Sub-critical Multiplication complex SM1 (figure 4.1) is located at the University of Pavia in the Radiochemistry Area of the Chemistry Department and has been mainly used in the past for research in radiochemistry since its installation in 1962.

For this work, the SM1 facility, in its original thermal configuration (i.e. with a water moderator), has been used as benchmark for reactor physics and neutron kinetics studies. Furthermore analyzes were performed for a feasibility study for the conversion of the facility from thermal to fast neutron spectrum configuration (i.e. substituting the water moderator with a solid lead diffuser). In this new configuration, SM1 could be a research facility suitable to perform nuclear transmutation studies for the long-lived elements in nuclear waste and to perform preliminary measurements and experiments for the validation of computational codes used for the analysis of sub-critical fast-neutron installations.



Figure 4.1: SM1 complex top view

In the first part of this chapter we report the work that was focussed on the validation of the model of the SM1 complex in its current thermal neutron configuration. The complex has been simulated by means of the Monte Carlo code MCNP and the multiplicative coefficient ( $k_{eff}$ ) and the neutron flux distributions have been evaluated inside the complex. For two specific in-core irradiation channels, measurements of the neutron fluxes have been performed by means of the foils activation and spectrum de-convolution technique based on the SAND II code and the results were used to benchmark the Monte Carlo model of the facility. Once validated the SM1 model for the thermal configuration, the second part work carried out focuses on the study, by means of Monte Carlo codes, of the neutron flux distribution and of the multiplicative coefficient in the SM1 converted to fast neutron spectrum. The benchmark of this Monte Carlo model would require the modification to a fast neutron spectrum configuration of the plant by substituting water moderator with a solid lead diffuser.

## 4.1 Experimental facility description

The SM1 facility is a thermal sub-critical complex moderated with light water. Fuel elements are assembled in an hexagonal prism geometrical configuration (figure 4.2) with a radial dimension of 114 cm and an height of 135 cm. The fuel is natural uranium in metallic form. In the SM1 thermal configuration considered for this study there are 206 Aluminum-clad fuel elements with an inner diameter of 2.8 cm and a length of 132 cm. The number of fuel elements in each lattice ring is reported in table 4.1.

Lattice ring	N° of fuel elements
1	6
2	11
3	18
4	23
5	30
6	35
7	42
8	41
9	0
Total	206

Table 4.1: Number of fuel elements in each of the nine core rings

Each fuel element is filled with five metallic Uranium ingots of cylindrical shape (inner diameter 2.74 cm and length 21.5 cm). Figure 4.2 shows the top view of the SM1 facility structure. The support grid has an hexagonal configuration for fuel elements holding (figure 4.2 – right) and in the centre it is located the neutron source whose support is schematically represented in figure 4.2 (left). The casing of the core tank is made of aluminium filled up with paraffin (20 cm thickness). Figure 4.3 shows the equatorial section of the SM1 core and in an x-y coordinate system with the origin located at the neutron source, the two irradiation channels have the following coordinates: A ( $x = 6.21$  cm,  $y = -4.40$  cm), B ( $x = -15.24$  cm,  $y = 8.80$  cm).

#### 4. Characterization of the SM1 subcritical Multiplying complex

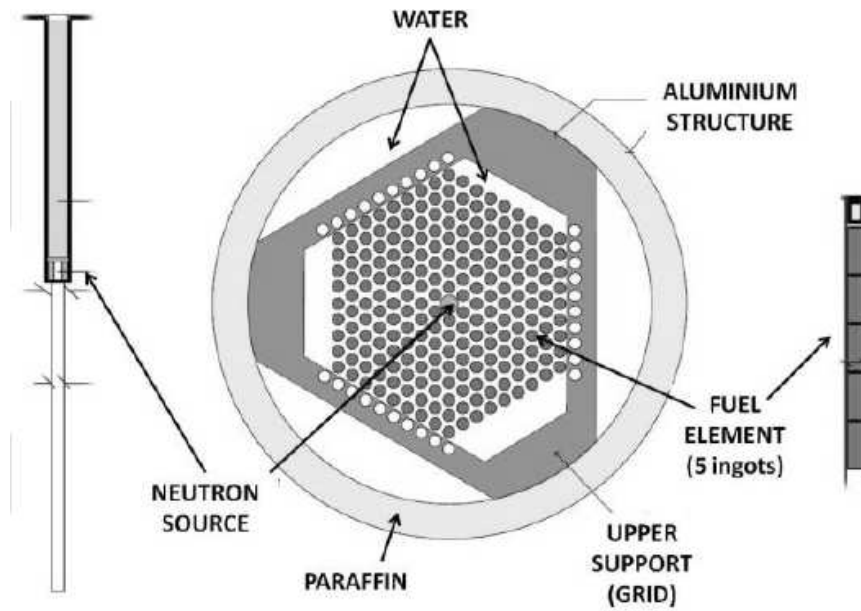


Figure 4.2: Top view of the SM1 model (centre of the figure). On the left: the neutron source with its support. On the right: fuel element composed of five ingots of natural Uranium inserted in the Aluminium cladding

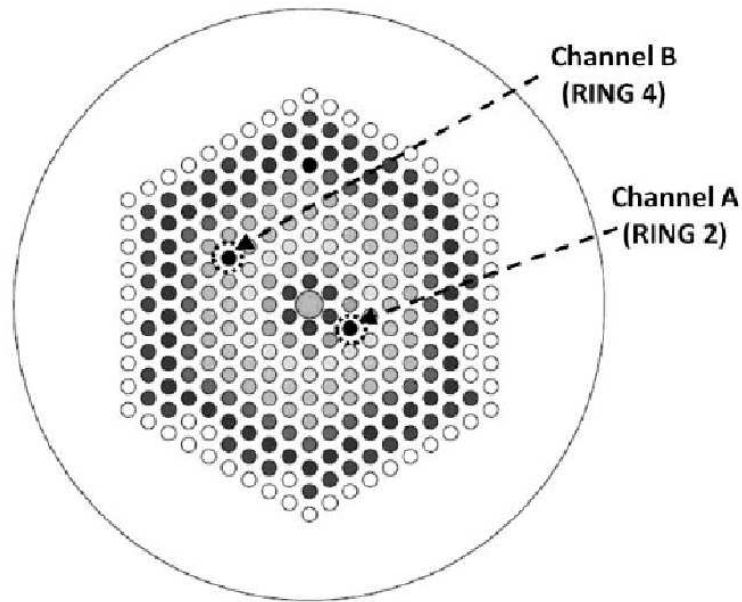
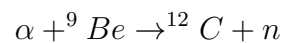


Figure 4.3: Scheme of the fuel element grid and irradiation channel positions A and B, in ring 2 and 4, respectively. The grey circle at the centre of the grid represents the neutron source position

The Pu-Be injecting neutron source, located at the center of the SM1 core has an emission yield of  $8.9 \times 10^6 \text{ n s}^{-1}$  over the  $4\pi$  solid angle. The source neutron spectrum, represented in figure 4.4, has been used as input in MCNP calculation in order to simulate the neutron injection.

$^{239}\text{Pu}$  during its decay emits  $\alpha$  particles and the neutron production is based on the  $(\alpha, n)$  nuclear reaction:



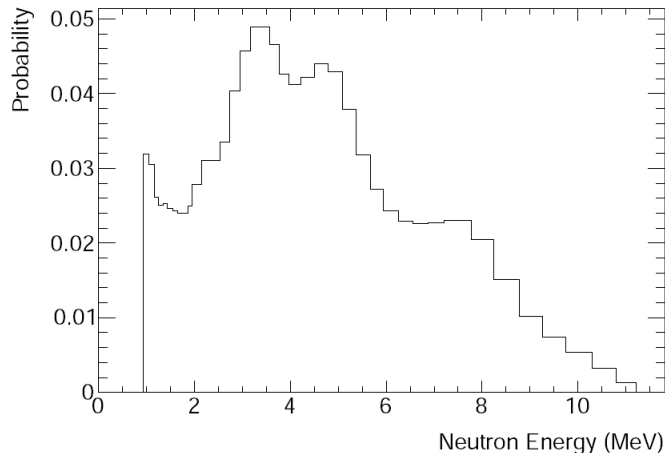


Figure 4.4: Pu-Be source neutron spectrum used as input for the source simulation with MCNP

## 4.2 Neutron flux simulations

The calculation of the neutron flux distributions [23] has been performed by means of MCNP. Since the sub-critical assembly is well below criticality (i.e.  $k_{eff} < 1$ ) the SDEF (Source definition) input card mode (i.e. fixed source mode) was used to model the neutron source and the neutron transport inside the lattice. For each MCNP run, a number of  $5 \times 10^8$  starting neutrons have been used to ensure good Monte Carlo statistics (no variance reduction techniques have been used in these simulations). The value of the effective multiplicative coefficient  $k_{eff,T}$  (where the subscript T stands for Thermal) of the complex in the thermal configuration was computed using the following equation

$$k_{eff,T} \cong k_{eff,T}^{FS} = \frac{N - 1}{N - \frac{1}{\bar{\nu}}} \quad (4.1)$$

where N is the Net Multiplication Factor (given by the output of each Monte Carlo run) defined by the relation

$$N = 1 + G_f + G_x \quad (4.2)$$

### 4.3. Neutron flux measurements

---

where  $G_f$  is the gain in neutrons from fissions,  $G_x$  is gain in neutrons from non-fission multiplicative reactions, and  $\bar{\nu}$  is the average number of emitted neutrons per fission (the superscript FS in formula 3.2 indicates the Fixed Source mode). All three parameters were evaluated by MCNP and a value of  $k_{eff,T} = 0.88 \pm 0.01$  was obtained which was in good agreement with the historical data reported in the licensing documentation of the facility ( $k_{eff,T} = 0.86$ ). The values of the integral neutron flux in the thermal configuration obtained by the MCNP simulations in each irradiation channel are reported in table 4.2

Irradiation channel	Integral neutron flux ( $n\text{ cm}^{-2}\text{s}^{-1}$ )
A	$(5.716 \pm 0.004) \times 10^4$
B	$(2.573 \pm 0.003) \times 10^4$

Table 4.2: Values of the integral neutron flux in each irradiation channel obtained with MCNP simulations

Using the fission density parameter calculated with MCNP for each ingot in the SM1 core it was also possible to calculate the total thermal power generated by the complex. To this purpose the following values have been used: volume of a single ingot of Uranium =  $126.5\text{ cm}^3$ , mean energy released per fission =  $202.5\text{ MeV}$  and neutron source intensity  $I = 8.9 \times 10^6\text{ n/s}$ . A value of the thermal power of the SM1 complex equal to  $P = 9.52 \times 10^{-4}\text{ W}$  was obtained.

### 4.3 Neutron flux measurements

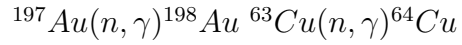
In order to validate the Monte Carlo simulations of the SM1 complex in its thermal-neutron configuration, measurements of the neutron flux distribution inside the irradiation channels of the complex have been performed by means of the foils activation and spectrum de-convolution technique based on the code SAND II (as reported in par. 3.2).

Irradiated foils were analyzed by means of INAA (Instrumental Neutron Activation Analysis) technique that is commonly used to determine the concentration of trace and major elements in a variety of matrices. Two irradiation positions inside the SM1 complex, whose positions are indicated in

#### 4. Characterization of the SM1 subcritical Multiplying complex

---

figure 4.3, were available for measurements. Considering the irradiation and measurement time optimization as well as radiation protection constraints, the following target has been selected



For each irradiation batch, two foils of the same material have been inserted in the two available irradiation channels. After each irradiation (5 in total for each position), measurements of the induced activity in the Copper and Gold target foils were performed by means of high resolution gamma-ray spectrometry (on a low-background HPGe coaxial and vertical dip-stick detector (EGG ORTEC), which has a relative efficiency of about 30% and a resolution of 1.95 keV FWHM at 1.332 MeV. As an example, in figure 4.5 the gamma ray spectrum for a Gold foil irradiated in SM1 is shown. The gamma-ray acquisition system consists of MAESTRO multi-channel Analyzer (MCA) emulation software card, coupled to the detector via electronic modules, all manufactured by EGG ORTEC. The multi-purpose gamma ray analysis software Gamma Vision was used for peaks identification and evaluation. In particular, the irradiation of each foil required about 2 weeks to reach activity at saturation corresponding to an irradiation time of about 5 half-lives.

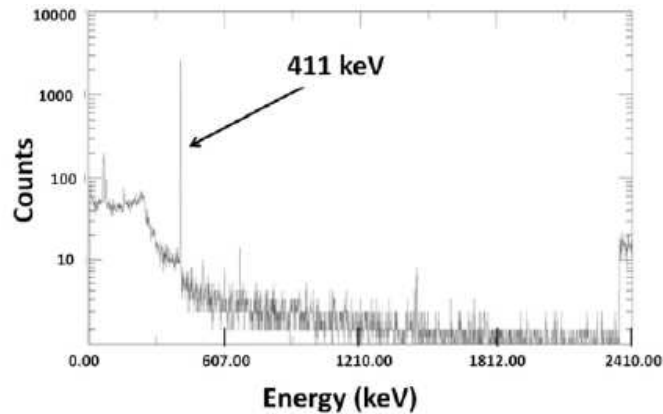


Figure 4.5: Measured gamma spectrum from one of the Gold foil irradiated in the SM1 complex. The arrow indicates the peak at 411 keV of the decay of  $^{198}\text{Au}$  used to calculate the neutron induced activity

### 4.3. Neutron flux measurements

---

The methodology used to calculate the specific saturation activity (SSA) of each foil and the attenuation coefficient of Gold foils are the same described for TRIGA reactor in sections 3.2.1 and 3.2.2.

The calculated specific activities at saturation for both Gold and Copper reactions, have then been used as input data for the SAND II program [24], [25]. Briefly, the SAND II computer code was developed to provide a best fit neutron flux distribution for a given input set of infinitely dilute foils specific activities (or specific activities for non dilute foils corrected by the attenuation coefficient, as explained above) using an iterative process. Starting from a guess flux (in our case the flux evaluated by means of MCNP), at each iteration the SAND II code calculates the infinitely dilute foils activities and compares them with the measured values and with the calculated values of the previous iteration. Using a complex algorithm, SAND II generates a set of correction values, one for each energy interval in which the neutron flux is divided, that are used to modify the flux calculated in the previous iteration. When the difference between the calculated activities and the measured activities is less than a value entered as input data in the SAND II (e.g. 5%), the iterative process stops. At the end of the calculation, the SAND II code gives a differential neutron flux distribution tabulated over 621 energy points, between  $10^{-10}$  MeV and 18 MeV. Unfortunately, the SAND II program does not calculate the uncertainties associated with the differential neutron spectrum. Thus, the method adopted in this work to calculate the propagation of the statistic uncertainties of the foils measurements into the de-convolution process, is based on a multiple run (100 for each of the two irradiation position) of the SAND II program with different sets of “measured” specific activities at saturation as input data. In order to produce this set of data, a set of 100 values fitting a Student’s t-distribution with mean equal to the mean measured specific activity itself, for each foils, and standard deviation equal to the measurement uncertainty was calculated. Thus, the SAND II program was run one hundred time for each irradiation position (i.e. position A and B) using, for each run, an input data set of specific activities at saturation previously calculated according to the Student’s t-distribution. The program was set in order to accept the result when the difference between the calculated and the measured activities was less than the total uncertainty associated to the gamma spectrometry measurements which has been estimated to be 5%

(statistical plus systematic contribution) for the analyzed peaks.

In table 4.3 are reported the mean specific saturation activities for Gold and Copper foils after the irradiation in channels A and B.

Irradiation channel	Gold SSA(Bq)	Copper SSA (Bq)
A	$4.1 \times 10^{-18}$	$7.1 \times 10^{-20}$
B	$2.1 \times 10^{-18}$	$3.7 \times 10^{-20}$

Table 4.3: Mean values of specific saturation activities for Gold and Copper foils for A and B irradiation channels

For each irradiation position, a set of one hundred neutron flux differential densities were evaluated, each one distributed over 621 energy points. Then, the average value of the flux differential density and the variance were evaluated in each energy point in order to obtain, for each irradiation position, an average flux differential density with a standard deviation. This approach was chosen in order to be able to propagate directly, into the de-convolution process, the uncertainties of the measurements of the activated foils [26]. In figures 4.6 and 4.7, the SAND output spectra obtained through this process, lumped into 69 energy groups, are compared with the neutron spectra obtained from MCNP calculations (also presented in 69 energy groups) .

In table 4.4 are reported the neutron flux values for both irradiation channels evaluated with SAND code

Irradiation channel	Integral neutron flux ( $n \text{ cm}^{-2}\text{s}^{-1}$ )
A	$5.74 \times 10^4 \pm 0.02$ (stat) $\pm 0.29$ (syst)
B	$(2.70 \times 10^4 \pm 0.01$ (stat) $\pm 0.14$ (syst)

Table 4.4: Values of the integral neutron flux in each irradiation channel obtained with SAND

Flux uncertainties are the same described in section 3.2.3 without the contribution of power calibration.

### 4.3. Neutron flux measurements

---

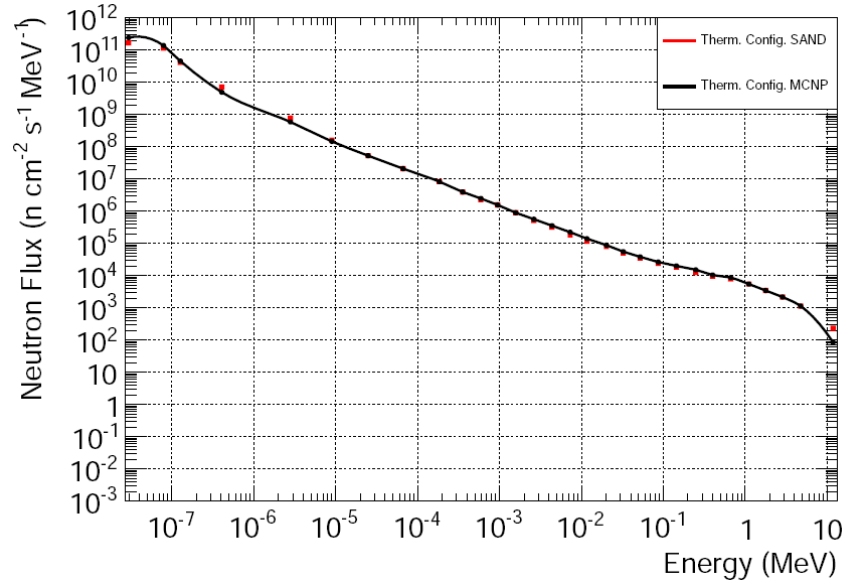


Figure 4.6: Comparison between measured obtained by processing the experimental data with the SAND II code) and simulated differential neutron fluxes (channel A) for SM1 in thermal configuration (Related errors are limited to the symbols)

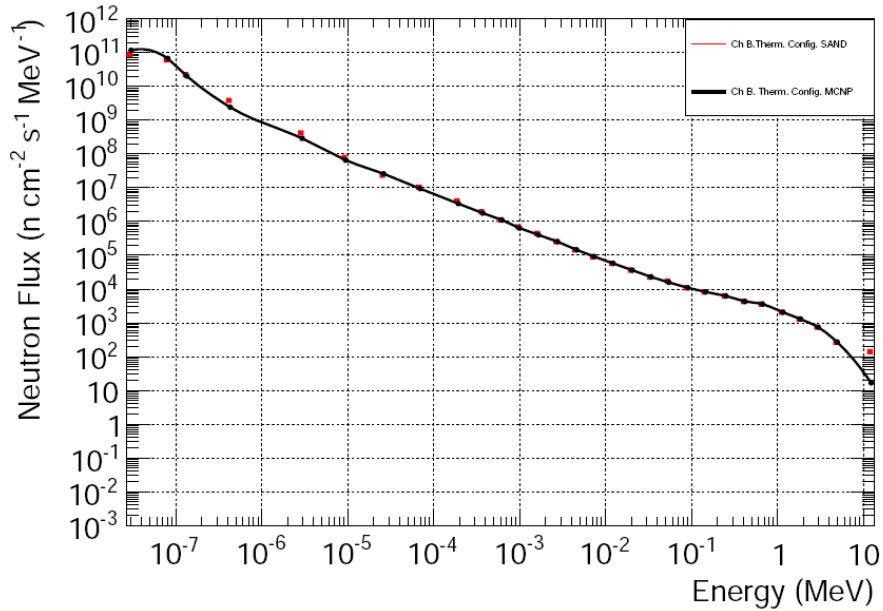


Figure 4.7: Comparison between measured and simulated differential neutron fluxes (channel B) for SM1 in thermal configuration (Related errors are limited to the symbols)

## 4.4 Fuel burn-up calculation

In this paragraph will be described the SM1 fuel burn-up calculation using analytical formulas and MC codes.

### 4.4.1 Burn-up analytical evaluation

In order to have an analytical burn-up evaluation the same methodology described in section 3.3, (considering ring by ring) have been used there. Using MCNP code the effective absorption and fission cross sections may be calculated for each core ring as reported in table 4.5

#### 4.4. Fuel burn-up calculation

---

Ring	$\sigma_f^{eff}$ (b)	$\sigma_{abs}^{eff}$ (b)
1	97.3	80.7
2	104.7	89.5
3	108.2	89.5
4	109.4	89.8
5	115.8	96.3
6	117.6	97.1
7	119.1	99.7
8	132.3	99.6

Table 4.5: Effective cross sections values for each SM1 core ring

Considering reactor time of operation of 36 years, the  $^{235}\text{U}$  consumed mass has been analytical calculated using the following formula:

$$N_i^{cons}(t) = N_{0,i}(1 - e^{-\sigma_a \phi t}) \quad (4.3)$$

calculated for each of eight core rings.

The comparison between the simulations and the analytical solutions is shown in table 4.6.

Ring	$^{235}\text{U}$ cons. mass (g) (an.)	$^{235}\text{U}$ cons. mass (g) (sim.)
1	$(7.30 \pm 0.01) \times 10^{-6}$	$(7.27 \pm 0.01) \times 10^{-6}$
2	$(1.03 \pm 0.01) \times 10^{-5}$	$(1.03 \pm 0.01) \times 10^{-5}$
3	$(1.25 \pm 0.01) \times 10^{-5}$	$(1.25 \pm 0.01) \times 10^{-5}$
4	$(1.30 \pm 0.02) \times 10^{-5}$	$(1.27 \pm 0.02) \times 10^{-5}$
5	$(1.30 \pm 0.02) \times 10^{-6}$	$(1.28 \pm 0.02) \times 10^{-5}$
6	$(1.10 \pm 0.02) \times 10^{-5}$	$(1.08 \pm 0.02) \times 10^{-5}$
7	$(9.01 \pm 0.03) \times 10^{-6}$	$(9.06 \pm 0.03) \times 10^{-6}$
8	$(6.40 \pm 0.03) \times 10^{-6}$	$(6.43 \pm 0.03) \times 10^{-6}$
Total	$(8.25 \pm 0.14) \times 10^{-5}$	$(8.19 \pm 0.14) \times 10^{-5}$

Table 4.6:  $^{235}\text{U}$  mass consumed in each core ring

#### 4. Characterization of the SM1 subcritical Multiplying complex

---

In order to calculate reactor burn-up (the mass of  $^{235}\text{U}$  consumed only by fission process), it is necessary to multiply consumed  $^{235}\text{U}$  mass to the ration between fission and absorption effective cross section in each ring

$$N_i^{fiss}(t) = N_{0,i} (1 - e^{-\sigma_a \phi t}) \frac{\sigma_{(f,i)}^{eff}}{\sigma_{(a,i)}^{eff}} \quad (4.4)$$

The results are reported in table 4.7

Ring	$^{235}\text{U}$ cons. mass (g) (an.)	$^{235}\text{U}$ cons. mass (g) (sim.)
1	$(6.05 \pm 0.01) \times 10^{-6}$	$(6.03 \pm 0.01) \times 10^{-6}$
2	$(8.75 \pm 0.01) \times 10^{-6}$	$(8.75 \pm 0.01) \times 10^{-6}$
3	$(1.07 \pm 0.01) \times 10^{-5}$	$(1.08 \pm 0.01) \times 10^{-5}$
4	$(1.06 \pm 0.02) \times 10^{-5}$	$(1.05 \pm 0.02) \times 10^{-5}$
5	$(1.09 \pm 0.02) \times 10^{-5}$	$(1.07 \pm 0.02) \times 10^{-5}$
6	$(9.17 \pm 0.01) \times 10^{-6}$	$(9.14 \pm 0.01) \times 10^{-6}$
7	$(7.55 \pm 0.02) \times 10^{-6}$	$(7.60 \pm 0.02) \times 10^{-6}$
8	$(6.40 \pm 0.03) \times 10^{-6}$	$(6.37 \pm 0.03) \times 10^{-6}$
Total	$(7.01 \pm 0.13) \times 10^{-5}$	$(6.99 \pm 0.13) \times 10^{-5}$

Table 4.7:  $^{235}\text{U}$  burn-up in each core ring

In figure 4.8 is shown the comparison between analytical and simulated burn-up calculation in each core ring.

#### 4.4. Fuel burn-up calculation

---

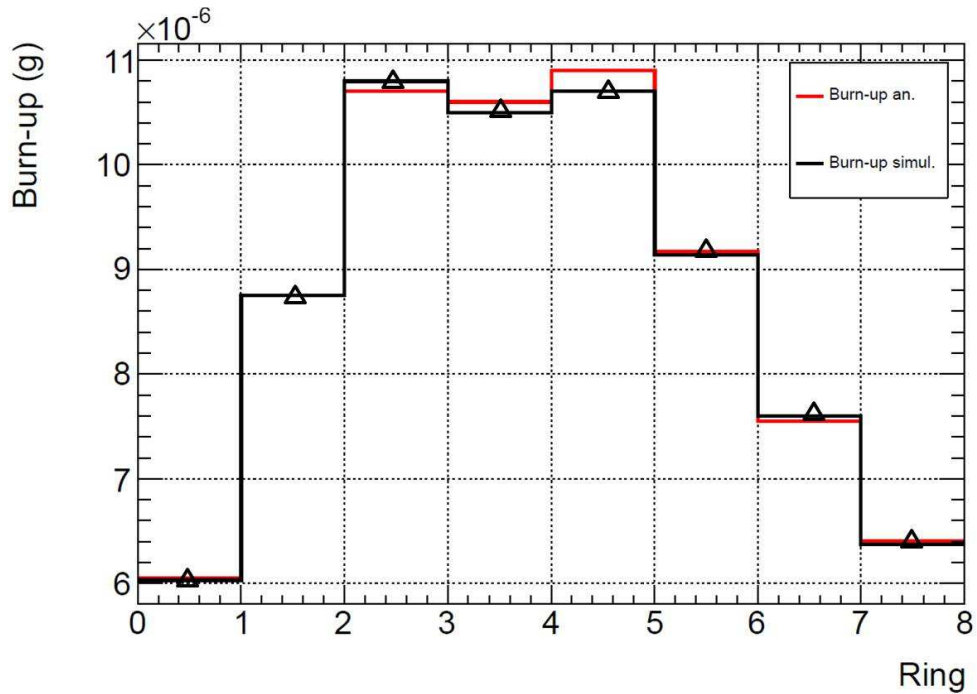


Figure 4.8: Comparison between analytical and simulated burn-up calculation in each core ring: errors are limited to the symbols

In order to have the diagonal fuel elements burn-up characterization have been performed some simulations considering  $^{137}\text{Cs}$  production in each of 5 ingots.

The results are shown in figure 4.9 in which the  $^{137}\text{Cs}$  activity behaviour of each ingot may be seen (ingot 1 is the closer to the top surface) ring by ring. The greater activity value found to be in the ingot 3 (neutron source level) while the activity in ingots 1 and 5 and in ingots 2 and 4, differently as expected, is not equal (cosine flux axial distribution) because neutron source is not perfectly positioned at fuel element equatorial level.

#### 4. Characterization of the SM1 subcritical Multiplying complex

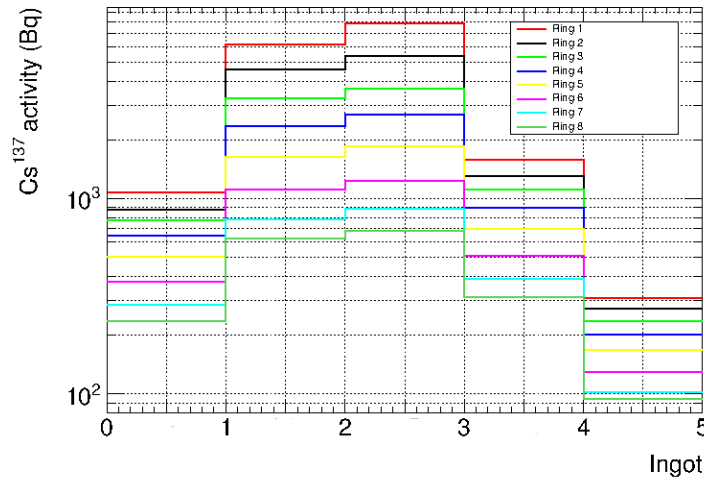


Figure 4.9:  $^{137}\text{Cs}$  activity in each of 5 ingots ring by ring

Neutron flux behaviour is shown in fig 4.10 ring by ring in each ingot.

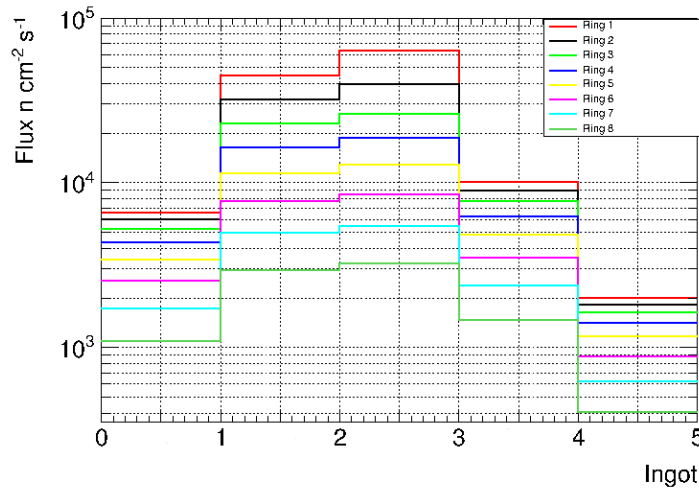


Figure 4.10: Neutron flux in each of 5 ingots ring by ring

$^{137}\text{Cs}$  activity has substantially the same neutron flux behaviour of each diagonal fuel element as shown in figure 4.11 for ring 1.

## 4.5. Feasibility study of SM1 conversion to lead fast reactor

---

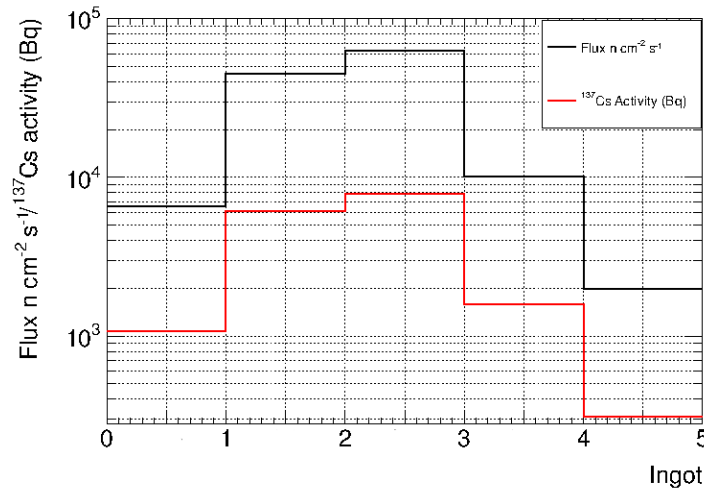


Figure 4.11: Neutron flux and  $^{137}\text{Cs}$  activity at ring 1 in each ingot

## 4.5 Feasibility study of SM1 conversion to lead fast reactor

Actually SM1 complex is in a light water thermal configuration, a feasibility study to possibly transforming it to lead fast reactor has been performed. A fast reactor has the characteristics shown in section 1.3.2.

This feasibility study deals with the search for the possible fast configurations [27], [28], two possibilities have been found:

- FE have been disposed in a lead brick reticulum (Fast 1)
- Keeping the same geometric disposition, the water has been substituted with solid lead spheres (Fast 2)

In figure 4.9 the top view of these two possible configurations are shown.

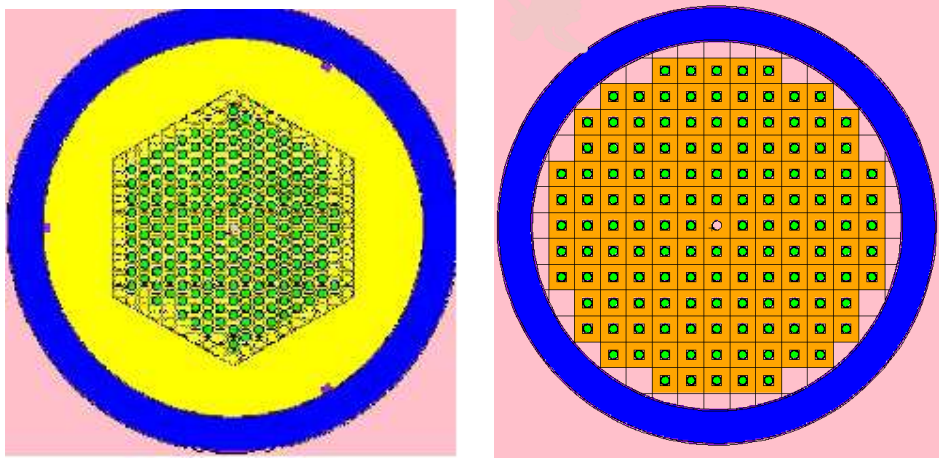


Figure 4.12: Top view of the two fast SM1 configurations; left panel: fast configuration in exagonal geometry (yellow represents lead). right panel: fast configuration with lead bricks (orange represents lead)

In table 4.8 are reported the characteristics of this two different fast configurations.

Characteristics	Fast 1	Fast 2
Diffuser	Lead grids	Lead spheres
FE	136 (680 ingots)	206 (1030 ingots)
Source	Pu-Be	Pu-Be
Source intensity	$8.9 \times 10^6$ n/s	$8.9 \times 10^6$ n/s
$k_{eff}$	$0.22 \pm 0.01$	$0.53 \pm 0.02$

Table 4.8: Fast configurations characteristics

In figure 4.13 we show the comparison between differential neutron fluxes collapsed in 69 energy groups in the irradiation channel A (present also in C2 configuration).

#### 4.5. Feasibility study of SM1 conversion to lead fast reactor

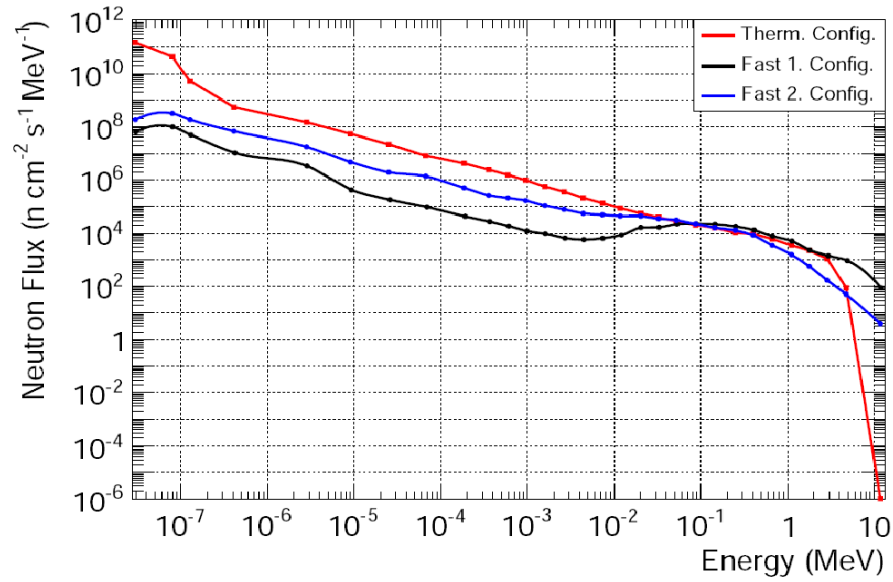


Figure 4.13: Differential fluxes for thermal and fast configurations in the position A

Integral flux in channel A in the different configurations (thermal and fast) is reported in table 4.9.

Conf.	Flux ( $\text{n cm}^{-2} \text{s}^{-1}$ )
Thermal	$(5.716 \pm 0.004) \times 10^4$
Fast 1	$(1.025 \pm 0.001) \times 10^4$
Fast 2	$(2.123 \pm 0.002) \times 10^4$

Table 4.9: Integral flux for different configurations

In figure 4.14 are shown the percentages of neutron flux in the thermal, epithermal and fast energy region with respect total integral flux.

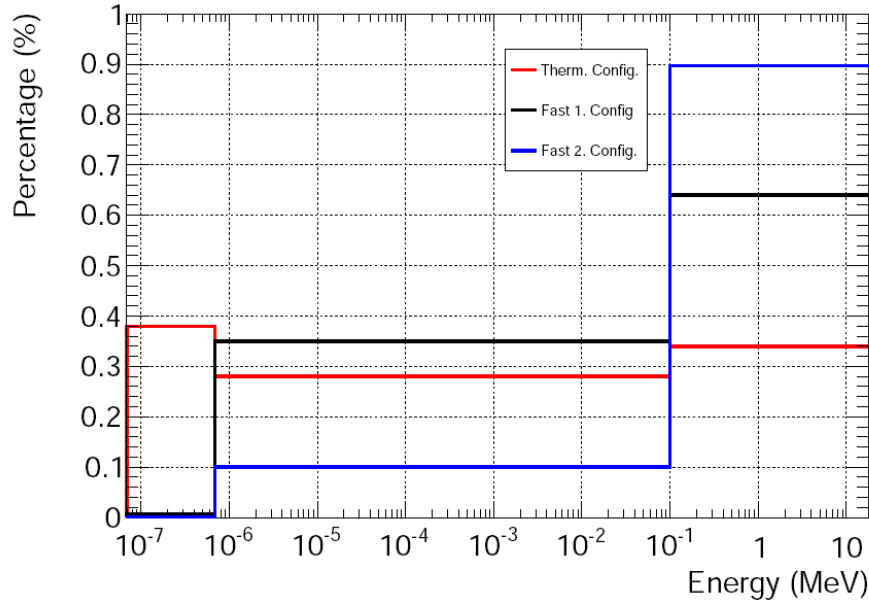


Figure 4.14: Percentages of neutron flux in the thermal, epithermal and fast energy regions with respect to total integral flux

As one can see, there is a percentage of thermal flux due to the paraffin external reflector, but in percentage the fast flux component is bigger than thermal and epithermal in both fast configurations.

From the results of these simulations it may at last be concluded that, as expected, the keff of the plant in the two fast configurations drops to a very low value (in both fast configurations described above) bringing the facility into a safer operational condition. On the other hand, the integral values of the neutron fluxes in the irradiation channels decrease, in average, of a factor about 2.5. This loss, though is partially compensated by the fact that the distribution of the neutron spectrum is shifted towards higher energies, will allow to use the SM1 plant in the new configuration for preliminary research activities on fast-neutron nuclear complexes.



#### 4. Characterization of the SM1 subcritical Multiplying complex

---

# Conclusions and future perspectives

Aim of this work is the burn-up evaluation in the TRIGA MARK II reactor and in the sub-critical multiplying complex SM1 of the University of Pavia. The knowledge of the process of fuel consumption is fundamental in a nuclear reactor because it is connected with the reactor performances and safety. In particular, during reactor operation, the evaluation of each fuel element burn-up, allows to accomplish the constraints of the plant operation licence and the optimization the core management. When the fuel is removed from the core, the knowledge of the burn-up is a necessary information in order to plan and to put in action a correct fuel handling and management for the final disposal. Furthermore the knowledge of burn-up allow the fuel management in the core reactor in order to extend the reactor life. In order to evaluate this important parameter the codes MCB (burn-up) and MCNP (reactor kinetic) have been experimentally and analytically validated successfully. MCB is the most flexible code which allows the use of detailed complex geometry and of neutron source definition. The validation results shown in chapter 2 are in a good agreement with respect to the results from analytical and experimental data; there are some discrepancies between these values for some fission products but not for the nuclides used in this work. These discrepancy could be attributed to cross section and fission yields data bases present in the codes libraries. For example in the case of low production rate there is a big uncertainty on the knowledge of the fission yields.

Strictly related to burn-up evaluation is the knowledge of neutron flux inside the fuel elements. The MCNP simulated flux outcomes (for the TRIGA reactor and for the SM1 Facility) have been experimentally validated through Neutron Activation Analysis technique, measuring the induced gamma activity in different foils (chapter 3) in different irradiation positions. Afterwards the code has been used for the calculation of flux distribution inside the TRIGA and SM1 fuel elements.

For the TRIGA reactor, fuel burn up has been preliminarily evaluated solving analytically the systems of differential equations which describe the  $^{235}\text{U}$  time evolution (consumption). Neutron fluxes inside fuel and effective absorption and fission cross sections have been calculated using MCNP code. The comparison between analytical results, simulations (MCB) and energy release formula (see section 1.1.5), of the TRIGA burn-up values until 31/12/2008 is reported in table 4.10.

	Burn-up (g)
Analytical	$370.8 \pm 11.6$
Simulated	$362.1 \pm 3.6$
Energy release formula	350.5

Table 4.10: Comparison between TRIGA burn-up values

The estimation of the total amount of fissioned  $^{235}\text{U}$  is, within the uncertainties, in good agreement with the evaluation based on the approximate relation between burn-up and total energy released during reactor operation and with simulations.  $^{239}\text{Pu}$  contribution to total energy production was not considered but, since the average fuel burn-up of the Pavia reactor is quite low (about 10%), we estimate that the Plutonium contribution should be in the order of few percent. Thus, the calculation based on the total energy released during reactor operation, overestimates the amount of fissioned  $^{235}\text{U}$  of the same small percentage. On the other side, the microscopic cross sections were evaluated for a reactor core configuration totally assembled with of Al-clad fuel elements while the calculation of the burn-up considered also SST-clad fuel elements (about 1/3 of the total number of fuel elements operated in the reactor). Since in literature [21] it is reported that SST-clad fuel elements

have a slightly higher (few percent) fission cross section than Al-clad ones, the calculation based on Monte Carlo code overestimated, again of few percent, the total mass of  $^{235}\text{U}$  fissioned. The approach adopted in this work has to be considered as a “first approximation”, useful for a preliminary evaluation of fuel burn-up in a TRIGA type research reactor. In order to perform a more detailed study of fuel depletion, it will be necessary to rely on fuel depletion codes and this will be the next steps of this research activity.

In particular three different configurations have been considered: 1965, 2009 and 2012. The use of the MCB codemade possible the evaluation of the -TRIGA reactor fuel burn-up.

The neutron flux in each fuel element have been weighted with the irradiation time in each position in order to simulate the  $^{235}\text{U}$  consumption in each fuel element.

This evaluation has been experimentally compared with core excess measurements. Taking into account a constant offset of 0.42 \$ from the first configuration (1965) which can be attributed to materials impurities and geometric approximations, one obtains a good agreement within uncertainties between measurements and simulations as one can see from table 4.11.

Configuration	$\rho_{sim}$ (\$)	$\rho_{sim}$ -offset (\$)	$\rho_{meas}$ (\$)
16/11/1965	$3.44\pm 0.04$	$3.02\pm 0.04$	$3.02\pm 0.06$
20/01/2009	$2.90\pm 0.04$	$2.48\pm 0.04$	$2.45\pm 0.05$
20/01/2012	$2.67\pm 0.04$	$2.25\pm 0.04$	$2.26\pm 0.04$

Table 4.11: Measurements and simulations core excess reactivity results

In the case of SM1 sub-critical multiplying complex of the University of Pavia aim of the work was to evaluate, by means of direct measurements, the neutron fluxes distribution inside the reactor core and to benchmark the results of the measurements with the simulation of the complex performed by means of MCNP. The fluxes were measured using the thin target foils activation technique coupled with spectrum de-convolution technique based on SAND II code.

The comparison between simulated and measured neutron fluxes in channels A (ring 2) and B (ring 4) are shown in table 4.12.

Channel	Flux sim. (n cm <sup>-2</sup> s <sup>-1</sup> )	Flux meas. (n cm <sup>-2</sup> s <sup>-1</sup> )
A	$(5.716 \pm 0.004) \times 10^4$	$5.74 \times 10^4 \pm 0.02$ (stat) $\pm 0.29$ (syst)
B	$(2.573 \pm 0.003) \times 10^4$	$(2.70 \times 10^4 \pm 0.01$ (stat) $\pm 0.14$ (syst)

Table 4.12: Simulated and measured values of the integral neutron flux in irradiation channels A and B

Once validated the MCNP code for neutron fluxes, it is possible to calculate SM1 fuel burn-up considering the mean flux for each core ring; the results are reported in table 4.13.

Ring	<sup>235</sup> U cons. mass (g) (an.)	<sup>235</sup> U cons. mass (g) (sim.)
1	$(6.05 \pm 0.01) \times 10^{-6}$	$(6.03 \pm 0.01) \times 10^{-6}$
2	$(8.75 \pm 0.01) \times 10^{-6}$	$(8.75 \pm 0.01) \times 10^{-6}$
3	$(1.07 \pm 0.01) \times 10^{-5}$	$(1.08 \pm 0.01) \times 10^{-5}$
4	$(1.06 \pm 0.02) \times 10^{-5}$	$(1.05 \pm 0.02) \times 10^{-5}$
5	$(1.09 \pm 0.02) \times 10^{-5}$	$(1.07 \pm 0.02) \times 10^{-5}$
6	$(9.17 \pm 0.01) \times 10^{-6}$	$(9.14 \pm 0.01) \times 10^{-6}$
7	$(7.55 \pm 0.02) \times 10^{-6}$	$(7.60 \pm 0.02) \times 10^{-6}$
8	$(6.40 \pm 0.03) \times 10^{-6}$	$(6.37 \pm 0.03) \times 10^{-6}$
Total	$(7.01 \pm 0.13) \times 10^{-5}$	$(6.99 \pm 0.13) \times 10^{-5}$

Table 4.13: <sup>235</sup>U burn-up in each core ring

There is a good agreement between simulations using MCB code and analytical results calculated with effective fission and absorption cross sections from MCNP code.

As a first step, a possible new configuration conversion could be a configuration based on a lead grid geometry based on a lead grid geometry with a reduced number of fuel elements (Fast 1); another possible configuration will be based on the substitution of the water moderator with a solid lead diffuser, keeping the same number of fuel elements without varying the geometry of the complex (Fast 2).

The results of these simulations are shown in the table 4.14.

Conf.	Flux (n cm <sup>-2</sup> s <sup>-1</sup> )
Thermal	(5.716±0.004)×10 <sup>4</sup>
Fast 1	(1.025±0.001)×10 <sup>4</sup>
Fast 2	(2.123±0.002)×10 <sup>4</sup>

Table 4.14: Fast configurations characteristics

A second aim of this work was to evaluate, by means of MCNP, the effective multiplication factor and the neutron fluxes distributions inside the SM1 complex in the fast-neutron spectrum configurations. From simulation results we may conclude that, as expected, the  $k_{eff,F}$  of the plant in the two fast configurations drops to a very low values  $k_{eff,F1} = 0.22±0.01$  and  $k_{eff,F2} = 0.53±0.02$  bringing the facility into a safer operational condition. On the other hand, the integral values of the neutron fluxes in the irradiation channels decrease, in average, of a factor about 2.5. This loss is partially compensated by the fact that the distribution of the neutron spectrum is shifted towards higher energies, could allow to use the SM1 plant in the new configuration for preliminary research activities on fast-neutron nuclear complexes.

A concluding remarks on this work is that the results presented here, for what concerns burn up calculation for the Pavia TRIGA reactor, will be used in September 2013 for core reconfiguration in order to gain an higher core excess value and consequently allowing an extension of the core life.

This research activities have been supported by INFN within the Projects “ARCO – Analysis of Reactor Core” and Nuc-Smile (Nuclear Subcritical Multiplication Installation for Lead Experiment) and by ENEA-MSE within the PAR 2010 - Project 1.3.2.a.



# Appendix: gamma spectroscopy measures

The detector used for gamma spectroscopy is an HPGe (High Purity Germanium) ORTEC GEM-FX7025P4-CW with high energy resolution and a Lead shielding in order to reduce the natural background. The detector is cooled with Liquid Nitrogen, a scheme of a typical semiconductor detector is shown in figure 15.

This is a semiconductor detector, gamma radiation interacting with the sensible volume produces an electron-hole couples through the following processes:

- Photoelectric effect
- Compton effect
- $e^+ e^-$  pair production

The Germanium structure is formed by the valence and conduction bands, separated by an energetic gap  $E_g=0.7$  eV at the temperature  $T=300$  K. The energy lost by the photon is transferred to the electron which is able to pass in the conduction band. In these detectors, radiation is measured by means of the number of charge carriers set free in the detector, which is arranged between two electrodes. Ionizing radiation produces free electrons and holes; the number of electron-hole pairs is proportional to the intensity of the radiation. As a result, a number of electrons are transferred from the valence band to



Counting standard deviation is expressed as  $\sigma = \sqrt{N}$ , where N is the number of counts. FWHM and standard deviation are connected by the relation  $\text{FWHM}=2.35\sigma$ . The mean peak value is  $E_0=KN$ , proportional to the created charges. Standard deviation can be write as  $\sigma=K\sqrt{N}$ , the resolution is:

$$R = \frac{2.35}{\sqrt{N}}$$

The low ionization energy allow a good energy resolution because the is a big number of formed charge.

The efficiency of this detector is can be given by  $\epsilon(E) = \epsilon_i(E)\epsilon_g(E)$  where  $\epsilon_i$  is the intrinsic efficiency and  $\epsilon_g$  is the geometric efficiency.

Geometric efficiency is given by

$$\epsilon_g = \frac{\Omega}{4\pi}$$

$\Omega$  is the solid angle expressed as  $\Omega = 2\pi(1 - \frac{d}{\sqrt{d^2-r^2}})$ , where d and r are shown in figure 16.

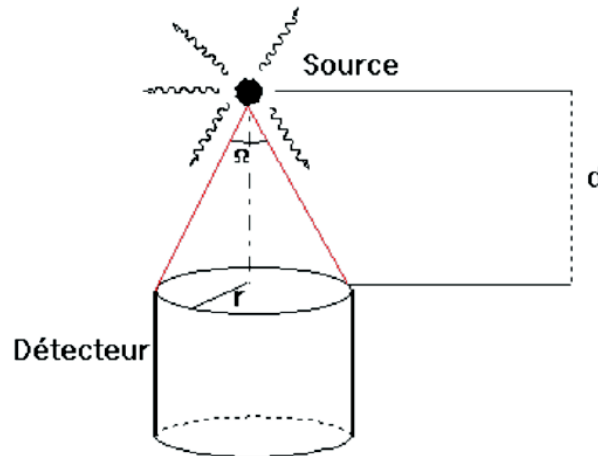


Figure 16: Schematic view of the parameters involved in the geometric efficiency

The efficiency can be expressed as

$$\epsilon_g(E) = \frac{N(E)}{A\eta(E)t}$$

where  $N(E)$  is the number of charges,  $A$  is the activity of the source,  $\eta(E)$  is the emission probability of each gamma ray and  $t$  is the counting time.

In figure 17 is shown the electronic chain for data acquisition.

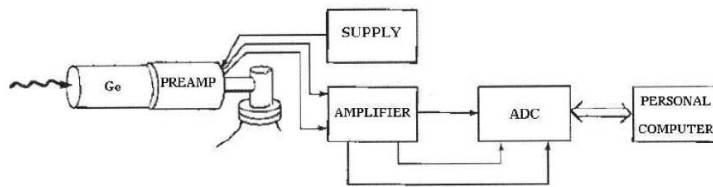


Figure 17: Data acquisition electronic chain

The electronic chain allow data acquisition on a personal computer, it is formed by a preamplifier with interface function between Germanium crystal and the acquisition electronics. The outcoming signal has an amplitude of few mV, so it is necessary an amplifier in order to have a greater voltage signal. The amplifier is connected with an ADC converter able to transform an analogic signal into a digital one. The chain ends with the ADC connected to a personal computer ready to collect all data from HPGe detector.





# Bibliography

- [1] M. A. Preston, R. K. Bhaduri, *Structure of the nucleus*, Addison Wesley publishing company, Massachusetts, 1975.
- [2] J. Eric Lynn, *Modern Fission Theory for Criticality*, Los Alamos National Laboratories, 2004.
- [3] John R. Lamarsh, *Introduction to Nuclear Reactor Theory*, Addison-Wesley Publishing Company, New York, 1972.
- [4] National Nuclear Data Center, *Evaluated Nuclear Data Files*, 2010.
- [5] Weston M. Stacey, *Reactor Safety, in Nuclear Reactor Physics, Second Edition*, Wiley-VCH Verlag GmbH Co. KGaA, Weinheim, 2007.
- [6] *International status and prospects of nuclear power*, IAEA report, Vienna, 2008.
- [7] M.Ash, *Nuclear Reactor Kinetics*, McGraw-Hill Inc.,US, 2nd edition August 1, 1979.
- [8] J. Cetnar, W. Gudowski, J. Wallenius, *User Manual for Monte-Carlo Continuos Energy Burn-up (MCB) Code - Version 1C*, 1997.
- [9] NIST *Standard Reference Database for Atomic Weights and Isotopic Compositions with Relative Atomic masses*, NIST Pub.

- [10] M. Dabbene, *Interpretazione di misure di attivazione per la valutazione del flusso neutronico nel reattore sperimentale TRIGA*, A.A. 2008/2009.
- [11] P.J. Griffin, et al., *User's Manual for SNL-SAND-II Code SAND-93-3957*, 1994.
- [12] Lieser, Karl H., *Nuclear and Radiochemistry*, 2nd Ed.: John Wiley Sons, Inc., 2001.
- [13] Alfassi, Z.B., *Chemical Analysis by Nuclear Methods*, John Wiley and Sons, Inc., 1994.
- [14] Lieser, Karl H., *Nuclear and Radiochemistry*, 2nd Ed.: John Wiley Sons, Inc., 2001.
- [15] Glenn F. Knoll, *Radiation Detection and measurement*, 1999.
- [16] Z.B. Alfassi, *Activation Analysis, Volumes I and II*, CRC Press: Boca Raton, FL., 1990.
- [17] D. De Soete, R. Gijbels, and J. Hoste, *Neutron Activation Analysis*, John Wiley and Sons: New York, NY., 1972.
- [18] A. Borio di Tigliole, F. Panza, J. Bruni, D. Alloni et al., *Preliminary TRIGA Fuel Burn-up evaluation by means Monte Carlo code and computation based on total energy released during reactor operation*, PHYSOR 2012 – Advances in Reactor Physics – Linking Research, Industry, and Education Knoxville, Tennessee, USA, April 15-20, 2012, on CD-ROM, American Nuclear Society, LaGrange Park, IL (2012).
- [19] M. Cagnazzo, D. Alloni, A. Borio, J. Bruni, G. Magrotti, S. Manera, F. Panza, M. Prata, A. Salvini, *Evaluation of the TRIGA reactor fuel burn-up by means of Monte Carlo codes and measurements*, presented at TRTR CONFERENCE 2012 - SAN DIEGO Ca.
- [20] RSICC COMPUTER CODE COLLECTION, *MCNP4C Monte Carlo N-Particle Transport Code System*, Los Alamos National Laboratory and Oak Ridge National Laboratory.

- [21] J. W. Sterbenz, Radionuclide Mass Inventory, Activity, Decay Heat and Dose Rate Parametric Data for TRIGA Spent Nuclear Fuel, Idaho National Engineering Laboratory 1997.
- [22] N. A. Hanan et al., *The use of WIMS-ANL lumped fission product cross sections for burned core analysis with the MCNP Monte Carlo code*, 1998.
- [23] A. Cazzola, *Caratterizzazione del flusso neutronico nel complesso moltiplicante sottocritico SM1 dell'Università di Pavia*, A.A. 2009/2010.
- [24] D. Alloni, A. Borio di Tigliole, J. Bruni, R. Cremonesi, M. Oddone, F. Panza et al., *Flux characterization in the SM1 sub-critical multiplying complex of the Pavia University*, Progress in Nuclear Energy 67 (2013) 98–103.
- [25] W.N. Mc Elroy et al., *A Computer-Automated Iterative Method for Neutron Flux Spectra Determination by Foil Activation*, Vol. 1 AFWL-TR 67-41, 1967.
- [26] S. Berg and W.N. McElroy, *A Computer-Automated Iterative Method for Neutron Flux Spectra Determination by Foil Activation*, Vol II: SAND II (Spectrum Analysis by Neutron Detectors II) and Associated Codes AFWL-TR-67-41, Vol.II 1967.
- [27] H. Nifenecker, S. David, J.M. Loiseaux, O. Meplan, *Basics of accelerator driven subcritical reactors*, Nuclear Instruments and Methods in Physics Research A, 463 (2001) 428–467.
- [28] H. Nifenecker, O. Meplan, S. David, *Accelerator Driven Subcritical Reactors Series in Fundamental and Applied Nuclear Physics Series*, CRC Press, 2003.
- [29] J. Bruni, *Valutazione del Burn-up del combustibile del reattore TRIGA Mark II del L.E.N.A. mediante codici di calcolo Monte Carlo e misure*, A.A. 2010/2011.
- [30] N. A. Hanan et al., *The use of WIMS-ANL lumped fission product cross sections for burned core analysis with the MCNP Monte Carlo code*, 1998.

- [31] A.Grisell, textitValidation of Monte-Carlo Continuous Energy Burnup Code (MCB) on Light Water Reactor Fuel, Stockholm 2004.





# List of publications

- D. Alloni, A. Borio di Tigliole, J. Bruni, R. Cremonesi, M. Oddone, **F. Panza** et al., *Flux characterization in the SM1 sub-critical multiplying complex of the Pavia University*, Progress in Nuclear Energy 67 (2013) 98-103.
- A. Borio di Tigliole, **F. Panza**, J. Bruni, D. Alloni et al., *Preliminary TRIGA Fuel Burn-up evaluation by means Monte Carlo code and computation based on total energy released during reactor operation*, PHYSOR 2012 – Advances in Reactor Physics – Linking Research, Industry and Education, Knoxville, Tennessee, USA, April 15-20, 2012, on CD-ROM, American Nuclear Society, LaGrange Park, Illinois (2012).
- M. Cagnazzo, D. Alloni, A. Borio, J. Bruni, G. Magrotti, S. Manera, **F. Panza**, M. Prata, A. Salvini, *Evaluation of the TRIGA reactor fuel burn-up by means of Monte Carlo codes and measurements*, presented at TRTR Conference 2012, San Diego California.



# Ringraziamenti

Desidero ringraziare il prof. Claudio Conta che, con saggezza e competenza, mi ha guidato nella stesura di questo lavoro di Tesi.

Ringrazio il dott. Ing. Andrea Borio di Tigliole, con il quale ho lavorato fianco a fianco e mi ha seguito in questo lavoro conclusivo del corso di Dottorato di Ricerca.

Un grazie sentito al dr. Daniele Alloni che mi ha sempre aiutato e seguito con simpatia e competenza non facendomi mai mancare il suo supporto tecnico e umano.

Grazie anche a tutto il personale del LENA, sempre disponibile e gentile per ogni necessità.

Un ringraziamento anche ai due lettori esterni, prof. Antonio Cammi e dr. Ing. Juan Esposito che si sono gentilmente prestati per questa importante attività.

Grazie al prof. Adalberto Piazzoli, le nostre chiacchierate sono sempre state simpatiche e soprattutto utili.

Grazie anche al dr. Andrea Rappoldi insostituibile punto di riferimento per il competente supporto informatico, alla prof. Carlotta Giusti e al prof. Franco Pacati, sempre disponibili e gentili per ogni dubbio e chiarimento di Fisica Nucleare e al prof. Paolo Pedroni sempre pronto a chiarire ogni questione di statistica.

Grazie anche al mio viciano di stanza, prof. Andrea Ottolenghi con il quale abbiamo trascorso momenti divertenti e dal quale ho sempre ricevuto utilissimi consigli.

Un sentito ringraziamento alla prof. Adele Rimoldi con la quale ho instaurato un'ottima collaborazione nell'ambito del tutorato del corso di Fisica sperimentale con laboratorio.

Ringrazio il prof. Mauro Carfora, coordinatore del corso di Dottorato di Ricerca, sempre preciso e disponibile ad ogni richiesta di chiarimento.

Grazie anche alla sig. Anna Rita Mangia e alla sig. Marina Ventura delle segretarie del Dipartimento di Fisica e dell'Istituto Nazionale di Fisica Nucleare (sez. di Pavia) sempre disponibili per ogni problema burocratico.

Grazie a Pierluigi, abbiamo trascorso tre anni ricchi di impegni, ma ci siamo anche tanto divertiti, grazie a Luca, con il quale il divertimento è assicurato in ogni nostro incontro.

Un ultimo grazie, ma non per questo meno importante, ai miei genitori, che mi hanno sempre supportato sotto ogni aspetto di questo percorso, dandomi sempre fiducia e appoggio incondizionati durante questa esperienza che mi ha dato davvero molto e mi ha fatto crescere sotto molti aspetti.